

1 **Title**
2 Interpreting the cause of bound earthquakes at underground injection experiments

3
4 **Authors**
5 Ryan Schultz^{1*}, Linus Villiger¹, Valentin Gischig¹, Stefan Wiemer¹

6
7 ¹ Swiss Seismological Service, ETH Zürich, Zürich, Switzerland
8 * corresponding author: Ryan.Schultz@sed.ethz.ch

9
10 **Abstract**

11 Constraining the maximum possible magnitude (M_{MAX}) of an induced earthquake
12 sequence is a challenging process with important implications for managing risks. CAP-tests
13 are a suite of statistical tests that can infer, quantify, and select best-fitting M_{MAX} models via
14 an earthquake catalogue's magnitudes. We use CAP-tests to discern between bound/unbound
15 earthquake sequences at underground laboratories, where high-resolution and near-field
16 geophysical observations are abundant. There, we find clear evidence for bound sequences,
17 where magnitude growth was restricted during stimulation. Furthermore, bound sequences
18 tend to be associated with stimulations that occurred within intact rock. On the other hand,
19 unbound sequences tended to be associated with stimulations where hydraulic fractures
20 interacted with relatively large pre-existing faults/fractures. We further examine bound
21 sequences by fitting magnitude growth to a generalized family of M_{MAX} functions. This
22 process appears to be able to aggregate bound sequences into categories consistent with
23 theoretical considerations (*e.g.*, tectonic, tensile-crack, or shear-crack). These results provide
24 a basis for validating and interpreting bound sequences in controlled experiments, which is
25 important for extrapolating to larger-scale observations. Overall, CAP-tests appear to be a
26 promising avenue for constraining M_{MAX} from earthquake catalogue data.

27
28 **Short Summary**

29 We use statistical tests to infer M_{MAX} from an earthquake catalogue and focus on data
30 from three underground laboratories with controlled injection experiments. There, we find
31 clear evidence for M_{MAX} bounds and corroborate interpretations of fracture growth against
32 other geophysical studies. Unbound sequences occur when stimulation is directed towards pre-
33 existing faults. The validation of our methods against well-studied cases is encouraging and
34 will help validate future interpretations.

35
36 **Key Points**

- 37
- Bound earthquake sequences (*i.e.*, physically restricted maximum magnitudes) were
- 38 unambiguously identified in underground laboratories.
- Bound sequences tend to be associated with stimulation stages, while unbound
- 39 sequences tend to inject into pre-existing faults/fractures.
- Maximum magnitudes aggregate into four categories that are consistent with
- 40
- Maximum magnitudes aggregate into four categories that are consistent with
- 41 theoretical expectations.
- 42
- 43
- 44

45 **Main text**

46 **1. Introduction**

47 Any process that has the potential to alter stresses in the subsurface also has the
48 potential to trigger earthquakes (Moein et al., 2023). To date, many types of anthropogenic
49 operations have induced earthquakes including wastewater disposal, hydraulic fracturing,
50 enhanced geothermal systems, geological carbon sequestration, reservoir impoundment, and
51 mining (Majer et al., 2007; Foulger et al., 2018; Schultz et al., 2020). In some cases, these
52 events have grown large enough to be felt, damaging, or even harmful (Atkinson et al., 2016;
53 Grigoli et al., 2018). In reaction to some of these cases, social concerns have resulted in
54 subsurface development moratoriums (Kettlety et al., 2021; Muntendam-Bos et al., 2022).

55 The need to manage the risks of induced earthquakes has been recognized (Bommer,
56 2022; Zhou et al., 2024). The *de facto* approach to risk management centralizes around the
57 traffic light protocol (Bommer et al., 2006), which delineates when an operation must stop (*i.e.*,
58 the red-light). Typically, red-lights are designed as magnitude thresholds (Schultz et al., 2021a;
59 2021b; 2023a). Despite the widespread adoption of traffic light protocols, relatively little is
60 understood about the growth of induced earthquake magnitudes. Some recent papers have
61 begun examining this topic; for example, by attempting to forecast the next largest event
62 (Mendecki, 2016; Cao et al., 2020; 2024; Schultz et al., 2023b; Verdon et al., 2023; 2024; Yin
63 et al., 2024). However, these approaches are unable to discern the adequacy of input models.
64 These topics are important for understanding trailing earthquakes (Schultz et al., 2022) and
65 magnitude jumps (Verdon & Bommer, 2021), which are among the most important factors for
66 designing risk-informed red-lights (Schultz et al., 2021a).

67 A common theme underlying these efforts is constraining the maximum possible
68 magnitude (M_{MAX}), given its prominence for induced seismicity hazard quantification
69 (Bommer & Verdon, 2024). While there are numerous theoretical models that could possibly
70 limit M_{MAX} (McGarr, 2014; Hallo et al., 2014; Galis et al., 2017; Elsworth, et al., 2025; Im &
71 Avouac, 2025; Sáez et al., 2025), there are relatively few methods available to reliably validate
72 them with empirical data (Holschneider et al., 2014; Pisarenko & Rodkin, 2022; [Kijko, 2025](#)).
73 In fact, empirically constraining M_{MAX} from a catalogue is known to be a challenging task that
74 is usually only possible in special circumstances (Holschneider et al., 2011; Zöller et al., 2016).
75 Given the conflict between needing M_{MAX} constraints against the lack of robust approaches,
76 expert solicitation is often used as a substitute (DeDontney et al., 2016). Thus, there is a need
77 to replace subjective/opinion-based methods with more quantitative measures for M_{MAX} .

78 Based on this need, CAP-tests were designed as a suite of statistical tests to infer and
79 quantify the presence of M_{MAX} within a catalogue of data. Specifically, this approach compares
80 the distribution of earthquake magnitudes (M) against the distribution of jumps in the largest
81 magnitude events (ΔM_{LRG}): when they are the same distribution, the catalogue is unbound and
82 there is no M_{MAX} (and *vice versa*) (Schultz, 2024). Synthetic testing suggests that this problem
83 reformulation can be more sensitive to M_{MAX} than traditional approaches (Schultz, 2024;
84 2026). CAP-tests are broken into three component parts: the KS-test ([Kolmogorov-Smirnov](#)
85 [test](#)) as a hypothesis test to infer the presence of M_{MAX} , the MLE-test ([Maximum Likelihood](#)
86 [Estimation test](#)) to quantify the value of M_{MAX} , and the EW-test ([Ensemble Weighting test](#)) to
87 select the theoretical M_{MAX} model that explains the catalogue data best. We provide the full
88 methodological details of CAP-tests in Section 2.

89 The application of CAP-tests to relatively larger magnitude induced seismicity cases
90 found that these cases behaved in an unbound manner (Schultz, 2024) – suggesting that the use
91 of theoretical M_{MAX} models (McGarr, 2014; Hallo et al., 2014; Galis et al., 2017; Elsworth, et
92 al., 2025; Im & Avouac, 2025; Sáez et al., 2025) are not appropriate during these fault
93 reactivations. On the other hand, smaller-scale cases of induced seismicity (e.g., Utah FORGE,
94 Preston New Road, Helsinki St1) from hydraulic stimulation indicated strong evidence for
95 bound magnitude growth via an M_{MAX} (Schultz et al., 2025). Furthermore, some stimulation
96 stages transitioned from a bound process into an unbound one; this was interpreted as these
97 particular stages reactivating pre-existing faults instead of stimulating new fractures. That said,
98 subsurface unknowns/uncertainties hamper an unambiguous interpretation for these field-scale
99 cases.

100 To better address subsurface unknowns/uncertainties, several underground laboratories
101 (UGLs) have performed hydraulic fracturing experiments with varying scales/scopes. These
102 intermediate-scale experiments aim to fill a gap between laboratory studies and field-scale
103 observations: accessing near-field geophysical observations (that are infeasible at the field-
104 scale) in a semi-realistic *in situ* setting. Said another way, UGL data was collected with the
105 intention of delineating and interpreting fracture stimulation. Thus, the complementary data
106 from UGLs is ideal for better interpreting bound sequences (found via CAP-tests). This
107 comparison has the potential to elucidate an underlying mechanism for bound induced
108 seismicity sequences. This [is](#) significant, since it starts to link statistical inferences of M_{MAX}
109 to physical processes.

110 In this study, we collect data from three UGLs: the Äspö Hard Rock Laboratory (Zang
111 et al., 2019; 2021), the Sanford Underground Research Facility (Dobson et al., 2018; Kneafsey

112 et al., 2018; Morris et al., 2018), and the Grimsel Test Site (Gischig et al., 2016; Amann et al.,
113 2018). We perform CAP-tests on these UGL datasets and observe both bound and unbound
114 stimulation stages. We cross-reference these observations against the wealth of geophysical
115 observations and interpretations from prior multi-disciplinary studies. Bound cases tend to
116 occur when stimulation is restricted to the growth of new fractures, while unbound cases tend
117 to reactivate (relatively large) pre-existing faults/fractures. Furthermore, we empirically search
118 for the functional form of M_{MAX} models; we delineate four categories that are predominantly
119 consistent with theoretical expectations. Finally, we discuss how these results create a
120 consistent picture with field-scale results.

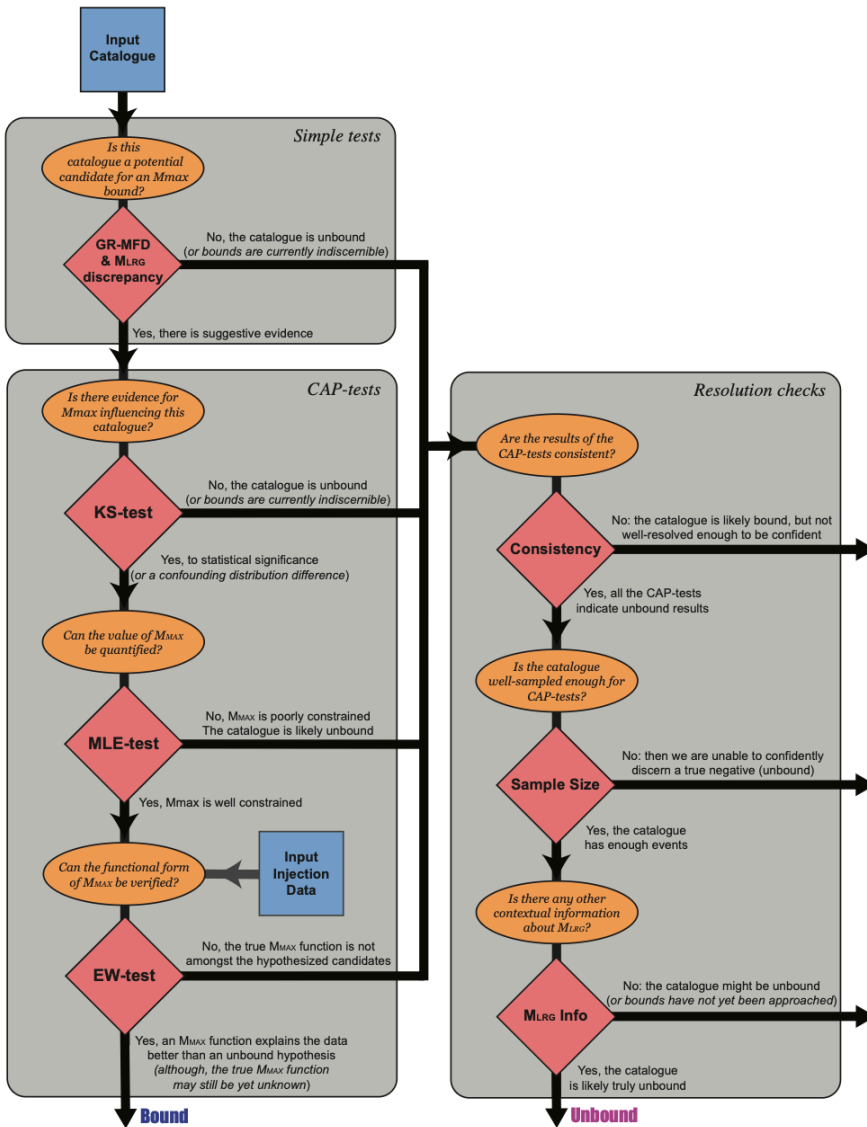
121

122 **2. Methods**

123 ***2.1 Methodological Overview***

124 The methods of this paper concern the robust inference and estimation of M_{MAX} from a
125 catalogue of earthquakes. To do so, we have composed a suite of statistical tests. First, simple-
126 tests can be used to pre-screen cases and provide qualitative or semi-quantitative inferences of
127 M_{MAX} bounds. Candidate catalogues can then be examined more deeply using CAP-tests,
128 which use a series of statistical tests to robustly discern the presence of M_{MAX} and quantify the
129 best model hypothesis. Last, we outline criteria for assessing the absence of M_{MAX} . These
130 tests are used to logically guide interpretations amongst the three possibilities: that M_{MAX}
131 bounds a catalogue, that M_{MAX} is not bounding a catalogue, or that the catalogue is not well-
132 resolved enough to make an interpretation either way. An overview of this workflow's logical
133 sequencing has been provided (Figure 1).

134



135
 136 **Figure 1. Workflow to discern M_{MAX} bounds.** Simple-tests are used to pre-screen for potentially
 137 bound catalogues. Afterwards, CAP-tests can more rigorously identify bound cases.
 138

139 **2.2 Simple-tests**

140 Here, we briefly define some simple-tests to provide an initial assessment of M_{MAX} .
 141 This is accomplished through an examination of the Gutenberg-Richter magnitude frequency

142 distribution (GR-MFD) (Ishimoto & Iida, 1939; Gutenberg & Richter, 1944) and discrepancies
143 between observed largest event minus the expected largest events. This sub-section constitutes
144 the first step in our overall workflow (Figure 1).

145

146 2.2.1 Fitting the Gutenberg-Richter Magnitude Frequency Distribution

147 The GR-MFD is a relationship that describes the amount and frequency of earthquake
148 magnitudes: $N = 10^a 10^{-bM}$. The a -value describes the scaling to the total amount of
149 earthquakes N , while the b -value is the proportionality of big-to-small events. Given a
150 catalogue of earthquake magnitudes M , this relationship can be fit through Maximum
151 Likelihood Estimators (Marzocchi & Sandri, 2003). For real datasets, a lower bound truncation
152 called the magnitude-of-completeness (M_c) is introduced to account for detection
153 incompleteness. Many methods exist to evaluate M_c robustly, to account for the
154 incompleteness in the detection of low magnitude events, thusly to avoid biases during the GR-
155 MFD fitting process. In this study, M_c is selected by searching for the value that maximizes
156 the goodness-of-fit metrics like R^2 (Schultz et al., 2018) or minimizes the negative log-
157 likelihood of the GR-MFD. In cases with a goodness-of-fit plateaus/valleys, we select the
158 value of M_c closest to plateau start. Sometimes we are conservative in our M_c choice by
159 selecting a value slightly larger than optimal. Note that this conservatism will have a
160 detrimental effect on finding bound cases. The M_c value selected by this process is typically
161 near (but skewed right-ward of) the peak bin of the non-cumulative GR-MFD.

162 As part of the simple indicators of M_{MAX} , a visual comparison of the GR-MFD fit
163 against the observed data is used to qualitatively examine for the presence of M_{MAX} .
164 Catalogues that are relatively deficient in large magnitudes (compared to their fits) are possible
165 candidates for an M_{MAX} . We note that this deficiency in large magnitude events is a key metric
166 for identifying if/when M_{MAX} can be constrained (Holschneider et al., 2011; Schultz, 2024;
167 [2026](#)).

168

169 2.2.2 Appraising the deficiency of large events

170 To provide additional semi-quantitative assessments of an M_{MAX} , we examine the
171 empirical degree-of-truncation (δM_{LRG}), which is the discrepancy between the largest observed
172 event minus the largest expected event. The expected M_{LRG} can be estimated: if a GR-MFD is
173 assumed, then order statistics suggests a modal value of $M_{LRG} = M_c + \log_{10}(N)/b$ (van der
174 Elst et al., 2016). Where N is the total number of events larger than the magnitude-of-

175 completeness M_c and b is the previously described b -value. We can use the prior GR-MFD
176 fits to determine the expected value of M_{LRG} and then compare that against the observed value
177 (*i.e.*, δM_{LRG}). We also use the inverted cumulative distribution function (van der Elst et al.,
178 2016) to determine the percentile of the δM_{LRG} discrepancy – or the likelihood of this degree-
179 of-truncation occurring, assuming an unbound catalogue.

180 As part of the simple indicators of M_{MAX} , catalogues that exhibit negative δM_{LRG}
181 suggest the presence of an M_{MAX} . We note that the δM_{LRG} discrepancy is a proxy metric for
182 the resolvability of CAP-tests. Usually values of $-0.5 M$ (or less) for $M_{LRG}-M_{MAX}$ are required
183 to confidently assert the presence of an M_{MAX} (Schultz, 2024; 2026). Note that this $M_{LRG}-$
184 M_{MAX} difference is the expected value where quantitative inferences of M_{MAX} can start being
185 made with 95% confidence, from theoretical considerations (Equation 15; Holschneider et al.,
186 2011).

187

188 **2.3 CAP-tests**

189 The CAP-tests are a suite of statistical methods aimed at discerning the influence of
190 M_{MAX} on a catalogue; each test is rooted in fundamentally different statistical frameworks, to
191 ensure the robust validation of results. In this sense, when all the CAP/simple-tests suggest a
192 similar bound/unbound result, we can be (more) confident that we have reached the right
193 interpretation – even if there might be data/method issues.

194 In this sub-section, we explicitly define each of the CAP-tests. We also refer readers
195 to a past study that defines the CAP-tests in detail, provides comprehensive sensitivity tests,
196 and highlight real-data applications (Schultz, 2024; Schultz et al., 2025; Verdon & Schultz,
197 2026). These tests build upon the simple pre-screening assessments (Section 2.2), logically
198 answering a sequence of questions to discern the influence of M_{MAX} more rigorously (Figure
199 1).

200

201 **2.3.1 The Kolmogorov-Smirnov test (KS-test)**

202 The first test is rooted in the statistical framework of hypothesis testing. Here, we take
203 advantage of the fact that the distribution of magnitudes (M) and the distribution of jumps in
204 the sequence of large events (ΔM_{LRG}) is the same if unbound, but differ when there is an M_{MAX}
205 upper bound (Schultz, 2024; 2026). This fact ideally lends itself to hypothesis testing via the
206 KS-test (Berger & Zhou, 2014). Given a catalogue, both M and ΔM_{LRG} can be observed. We
207 can then compare these two observations against each other to test if they are drawn from the
208 same distribution (or not), via the KS-test. This approach is advantageous in that it is non-

209 parametric – *i.e.*, it is completely data-driven and imposes no assumptions about the kind of
 210 distributions M or ΔM_{LRG} were drawn from. Because of this, we do not need to fit the data to
 211 a GR-MFD or have any knowledge/estimates of the b -value to perform our KS-test.
 212 Confidence in the KS-test is reported as compliments of standard p -values, where 95% is a
 213 common threshold used to declare statistical significance.

214 Since this test is only interested in discerning the existence of an M_{MAX} , additional
 215 catalogue realizations can be drawn through reshuffling the order of events. In this sense,
 216 bootstrapping can be employed to generate numerous catalogue realizations in which the KS-
 217 test is repeated. This provides more robust p -value estimates. Testing on both synthetic and
 218 real datasets suggests that the KS-test is significantly more sensitive to discerning M_{MAX} than
 219 approaches that attempt to appraise GR-MFD fits (Schultz, 2024; 2026). As well, synthetic
 220 testing on unbound cases shows that this KS-test produces false-positives at the rate expected
 221 for a p -value distribution (Schultz, 2024). To be able to discern the influence of M_{MAX} , M_{LRG} -
 222 M_{MAX} discrepancies of $-0.5 M$ or better are usually required, consistent with theoretical
 223 expectation (Holschneider et al., 2011).

224 While this formulation of the KS-test is powerful, we also provide a word of caution
 225 towards a potential interpretation pitfall: this method is testing for differences between the
 226 distributions M and ΔM_{LRG} . The presence of an M_{MAX} is one possible reason for this
 227 difference, but others may also confound a clear interpretation (*e.g.*, temporal changes in b -
 228 value, kinked distributions, tapered distributions). Thus, the KS-test should be suitably pre-
 229 processed or complemented with other tests to increase the certainty of an M_{MAX} interpretation.

230
 231

232 2.3.2 The Maximum Likelihood Estimator (MLE-test)

233 The next test is rooted in the statistical framework of Maximum Likelihood Estimation.
 234 If there is some suggestive evidence for the existence of an M_{MAX} , the next natural step is to
 235 quantify this value. The log-likelihood function is defined as follows:

$$236 \quad \ln(\mathcal{L}(M; \theta)) = \sum_i \ln(f_M(M; b, M_c, M_{\text{MAX}})) - \sum_j \ln(f_M(\Delta M_{\text{LRG}}; b, 0, M_{\text{MAX}} - M_{\text{LRG}}))$$

237 Where the probability density function of the GR-MFD is given by $f_M(M)$, with a set of model
 238 parameters θ (Schultz, 2024). This function essentially entails two parts: the log-likelihood
 239 for the catalogue magnitudes M (right-hand side of equation, first term) and the log-likelihood
 240 of the jumps in largest events ΔM_{LRG} (right-hand side of equation, second term). The optimal
 241 set of model parameters θ are then solved for via numerical methods to maximize the log-

242 likelihood, given the observed catalogue data M and ΔM_{LRG} . We perform this optimization in
243 two-steps: the first using the standard log-likelihood constrain the b -value (Marzocchi &
244 Sandri, 2003) (with the optimal M_c estimates) and then using the composite log-likelihood to
245 constrain M_{MAX} . In this study, we consider the simplest M_{MAX} variant for $f_M(M)$, which is a
246 truncated GR-MFD (Schultz, 2024).

247 If this test is only interested in discerning a stationary value of M_{MAX} , additional
248 catalogue realizations can be drawn through reshuffling the order of events. Similar to the KS-
249 test, bootstrapping can be employed to generate numerous catalogue realizations in which the
250 MLE-test is repeated. This provides more robust M_{MAX} estimates. Testing on both synthetic
251 and real datasets suggests that the MLE-test is sensitive to quantifying M_{MAX} within a
252 hundredth of a magnitude unit when $M_{\text{LRG}}-M_{\text{MAX}}$ discrepancies are $-0.5 M$ or better. In cases
253 where the MLE-test is applied to unbound catalogues, bootstrapped estimates of M_{MAX} will be
254 much larger than M_{LRG} and standard deviations can be on the order of 1 magnitude unit or
255 greater.

256

257 2.3.3 The Ensemble Weighting test (EW-test)

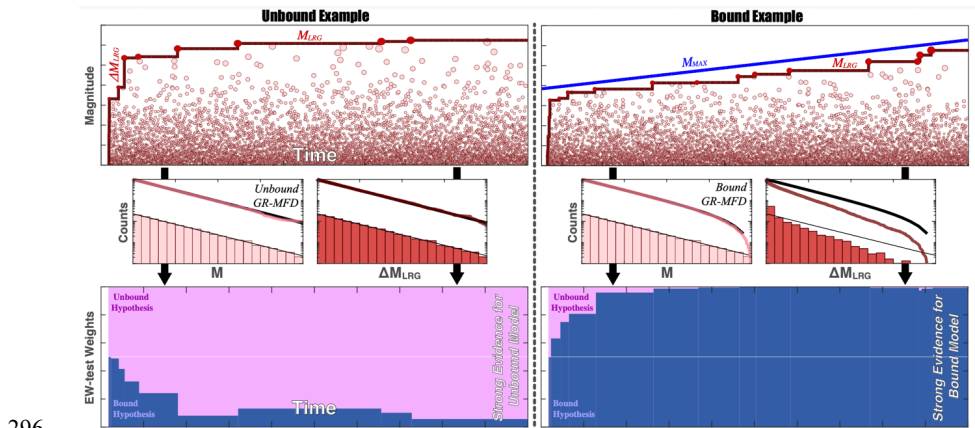
258 The third and final CAP-test is rooted in the statistical framework of likelihood
259 inference. Together, the two prior tests provide suitable evidence for the existence of M_{MAX} .
260 However, M_{MAX} may be a function of time or injected volume, becoming some non-stationary
261 value throughout the catalogue duration. Certainly, M_{MAX} processes relevant for induced
262 seismicity and hydraulic fracturing have been proposed in the past (McGarr, 2014; Hallo et al.,
263 2014; Galis et al., 2017; Elsworth, et al., 2025; Im & Avouac, 2025; Sáez et al., 2025). In this
264 sense, having an approach that can distinguish the best proposed M_{MAX} model (given the data)
265 would be insightful.

266 The EW-test starts by considering an ensemble of proposed M_{MAX} models to explain
267 the catalogue data (Schultz, 2024). Using the previously defined log-likelihood function, both
268 Akaike Information Criterion (AIC) and Bayesian Information Criterion (BIC) can be defined
269 for each M_{MAX} model (Schwarz, 1978; Akaike, 1998); note that we have used the small sample
270 size corrections for AIC/BIC (Sugiura, 1978; McQuarrie, 1999). Next, we compute the
271 differences in AIC/BIC scores, by subtracting the score of the best M_{MAX} model. These score
272 differences can be translated into relative model weights by an exponential function
273 (Wagenmakers & Farrell, 2004). We combine AIC/BIC weights into a single weight by taking
274 an average between the two. In this study we will consider four standard M_{MAX} models:
275 McGarr-like (*i.e.*, log-proportional to injected volume; $M_{\text{MAX}} \propto \log_{10}(V^1)$) (McGarr, 2014;

276 Hallo et al., 2014; Elsworth, et al., 2025), Galis-like (*i.e.*, $M_{\text{MAX}} \propto \log_{10}(V^{3/2})$) (Galis et al.,
 277 2017), a constant tectonic upper bound (Kanamori & Anderson, 1975), and the unbound null
 278 hypothesis. The unbound null hypothesis consists of three model parameters (M_c , b -value,
 279 GR-MFD variance), while all bound models have one additional model parameter (*i.e.*, $K=4$)
 280 to account for the slope of the volume-based relationship.

281 The interpretation of the M_{MAX} model weights is straightforward: larger model weights
 282 indicate a better explanation of the data. The model with the largest weight is the best
 283 explanation of the data (within the ensemble). To quantify the statistical significance of weight
 284 differences between two models, the relative odds ratio can be computed as the ratio of the two
 285 model weights (larger/smaller). Ratios of 1+ are insignificant, 3+ are substantial/positive, 10+
 286 are strong, and 100+ is decisive (Kass & Raftery, 1995). We note that the best model in an
 287 ensemble does not necessarily imply the veracity of the model; there could be another
 288 (unknown) model that explains the data better than all of those yet considered.

289 In synthetic testing, the EW-test can accurately and confidently discern the true M_{MAX}
 290 model (Schultz, 2024). Usually, only a handful of ΔM_{LRG} observations are required to
 291 confidently identify the true model (*i.e.*, with odds ratios of 3-10 or better). However, like the
 292 prior CAP-tests, M_{MAX} must be influencing the catalogue for meaningful inferences to be made.
 293 Said another way, if the M_{MAX} is much larger than M_{LRG} , then the EW-test will not be able to
 294 distinguish between bound/unbound hypotheses. A schematic diagram explaining the EW-test
 295 has been provided (Figure 2).



296
 297 **Figure 2. Schematic demonstration of the EW-test.** The upper panels show hypothetical catalogues
 298 of earthquakes. Earthquake magnitudes (M , pink circles), the sequence of largest events (M_{LRG} , red
 299 line), and jumps in the largest event magnitudes (ΔM_{LRG}) can be directly observed. Potentially, some
 300 unobservable physical process could be bounding these catalogues (M_{MAX} , blue line). Left and right

301 panels detail contrasting concepts for a bound and unbound catalogue, respectively. If there is an
302 M_{MAX} , then it can be statistically inferred from the observables. Middle panels show the differences
303 between distributions of M and M_{LRG} , when bounded by M_{MAX} (or not). The distribution of M follows
304 a GR-MFD: analytical cumulative (thick black line) and non-cumulative (thin black line) agree with
305 numerical cumulative (pink line) and non-cumulative (pink bars) distributions. The distribution of
306 ΔM_{LRG} will differ from the GR-MFD when bounded by M_{MAX} . Bottom panels show the results of EW-
307 tests using these concepts. Weights of two hypothesized models, an unbound M_{MAX} (pink area) and a
308 bound M_{MAX} (blue area), change as new values of M_{LRG} are observed. EW-tests can quickly infer the
309 presence of the true M_{MAX} model, from the equivocal *a priori* assumption (white horizontal line).
310

311 **2.4 Truly unbound or just lacking data?**

312 In an ideal experiment, injection would continue indefinitely, providing excellent
313 resolving power for M_{MAX} by sampling infinitely many large events near M_{MAX} . Obviously,
314 real-data cases are sample/time-limited, however. CAP-tests have the potential to discern
315 influence from M_{MAX} in a (sample-limited but still) well-resolved catalogue. However, an
316 issue arises when attempting to perform these tests on poorly-resolved catalogues, since CAP-
317 tests cannot distinguish an M_{MAX} in this case. For example, if CAP-tests fail to indicate a
318 bound catalogue, then this could be because the catalogue is either truly unbound or simply is
319 not well-resolved enough (*i.e.*, it has a low degree-of-truncation). Distinguishing between
320 these two possibilities can be nebulous. We outline some guiding metrics to assist in making
321 this assessment, which is our last workflow step in discerning the (apparent) absence of M_{MAX}
322 more rigorously (Figure 1).

323 The first consideration is the consistency among simple/CAP-test results. Cases that
324 are truly bound tend to have all tests unanimously indicate a bound process, and *vice versa*.
325 For reference, sensitivity testing on bound real-data that was sequentially decimated indicated
326 a loss of resolving power, consistent with the degree of decimation (Schultz et al., 2025).
327 Specifically, the EW-test tends to lose resolving power first, followed by the KS-test, with the
328 MLE-test generally being the most sensitive. In fact, the use of multiple sub-tests rooted in
329 disparate statistical methods was an intentional design choice to cover strength/deficiencies of
330 each individual approach (Schultz, 2024). Note that this consistency indicator is only relevant
331 for semi-well-resolved cases that are truly bound; very-poorly-resolved cases would still appear
332 as unbound.

333 The second metric considered is the size of the catalogue N , within 1-2 magnitude units
334 of the current M_{LRG} . Synthetic tests indicate that catalogues between 10^1 - 10^2 (above the M_c)
335 are usually required to confidently assert M_{MAX} (Schultz, 2024). Similarly, real-data cases also
336 noted that EW-tests can confidently assert an M_{MAX} model after observing 30-200 events –

Deleted: ²

Deleted: ³

339 although most cases required ~50-100 events (Schultz et al., 2025). Thus, we can use catalogue
340 size as another rough indicator for how well-resolved M_{MAX} is.

341 The third metric we will consider is the currently observed M_{LRG} . Specifically, we will
342 consider M_{LRG} in a contextual comparison against relevant cases that are already known to be
343 bound. For example, if two independent neighbouring stages (with similarly sized catalogues)
344 give diverging bound/unbound responses, then the observed M_{LRG} can be used to make
345 inferences. Scenarios where the unbound stage has an observed M_{LRG} greater than the bound
346 stage is more likely to be truly unbound. On the other hand, scenarios where the unbound stage
347 has an observed M_{LRG} significantly less than the bound stage is potentially just a poorly-
348 resolved case.

349

350 **3. Data, Results, & Interpretations**

351 We apply this workflow to data collected at a few UGLs that were aimed at better
352 understanding the hydraulic fracturing process (Figure 3). UGLs include the Äspö Hard Rock
353 Laboratory (Äspö HRL), Sanford Underground Research Facility (SURF), and the Grimsel
354 Test Site (GTS). Each of these UGLs had differing scopes, scales, and aims. Here, we will
355 cover each UGL in a parallel style: we introduce each UGL, examine CAP-test results at the
356 UGL, and then briefly interprets those results. We will start with the simpler UGLs and then
357 transition into more complex cases, to pedagogically build upon the complexity of
358 interpretations.

359



360

361 **Figure 3. Global locations of datasets.** Locations of the test sites considered: the Åspö Hard Rock
 362 Laboratory (Sweden), Sanford Underground Research Facility (South Dakota, USA), and the Grimsel
 363 Test Site (Switzerland). Supporting locations from past studies (Schultz, 2024; Schultz et al., 2025),
 364 are also shown.
 365

366 3.1 The Åspö Hard Rock Laboratory

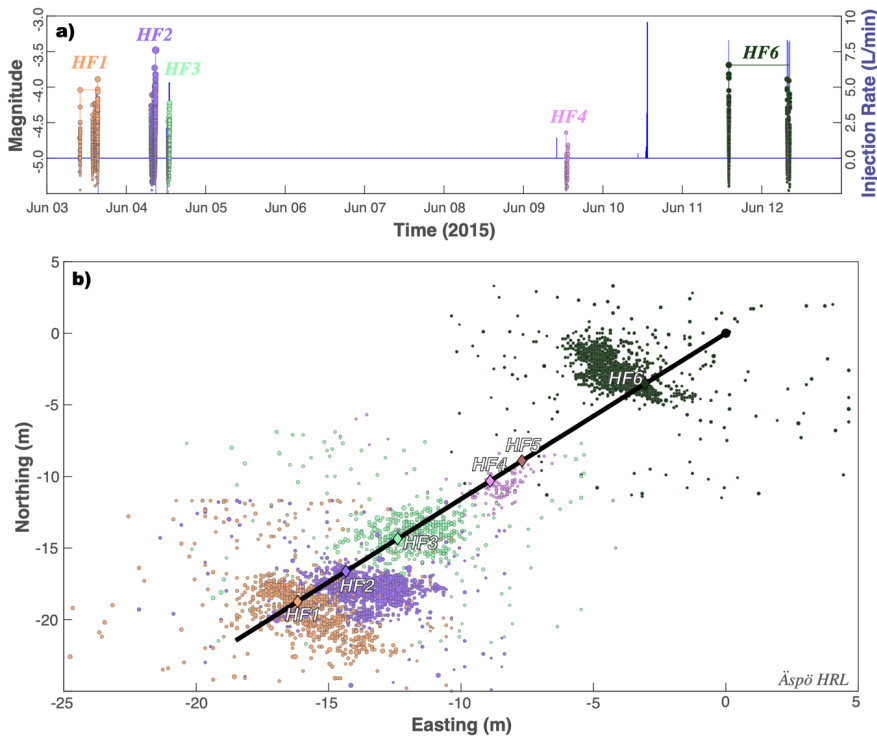
367 3.1.1 Overview of the Åspö HRL

368 The Åspö HRL is located on the Baltic east coast of Sweden, near the Simpevarp
 369 Peninsula (Figure 3). This UGL was constructed as a testbed to study the potential for nuclear
 370 waste storage by the Swedish Nuclear Fuel and Waste Management Company starting in 1986.
 371 By 1995, construction efforts reached the 450 m target depth into the granitoids of the Trans-
 372 Scandinavian Igneous Belt (Stanfors et al., 1999).

373 The intention of recent (June 2015) injection experiments at the Åspö HRL was to test
 374 the feasibility of cyclic stimulation as an alternative means to enhance subsurface permeability,
 375 while also reducing the severity of induced seismicity (Zang et al., 2019; 2021). Six injection
 376 stages (HF1-HF6) were conducted in a single borehole (28 m long at 410 m depth), with an
 377 average stage spacing of ~3 m, and encountering either Ävrö granodiorite or fine-grained
 378 diorite-gabbro. Stage locations were chosen to avoid natural fractures (Zimmerman et al.,
 379 2019). Each stage used between 4.1-27.2 L of injected fluid, spread between 4-6 injection sub-
 380 cycles (Zang et al., 2017; 2019). Some stages (HF1, HF2, HF4, & HF6) used traditional
 381 hydraulic fracturing techniques, while other stages (HF3 & HF5) employed cyclic stimulation
 382 (Zang et al., 2019). Resulting microseismicity was predominantly recorded in stages HF1-HF2

Deleted: 5

384 (López-Comino et al., 2017; Niemz et al., 2020; 2021), with events reaching up to M_w -3.5
 385 (Kwiatek et al., 2018) and slipping with reverse or strike-slip motions (López-Comino et al.,
 386 2021). Cyclic stimulations tended to produce less seismicity (Zang et al., 2019) and more
 387 complex fracture networks (Stephansson et al., 2019; Zhuang et al., 2019), albeit with less
 388 permeability enhancement (Zimmerman et al., 2019). Data for the Äspö HRL is publicly
 389 available (Zang et al., 2024) and a spatiotemporal summary of stimulation events is plotted
 390 (Figure 4).
 391



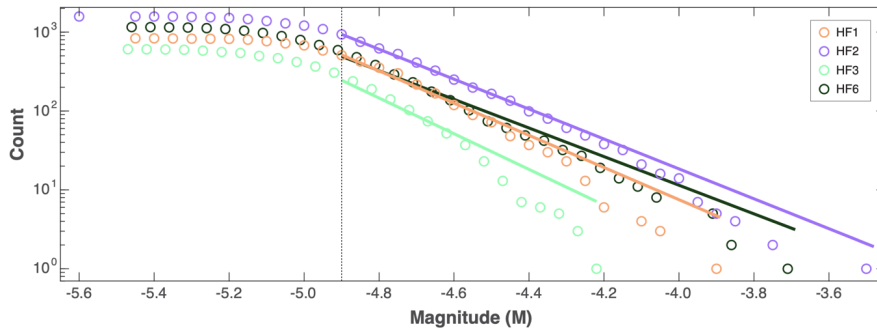
392 **Figure 4. Hydraulic stimulation and earthquake response at the Äspö HRL.** a) Timings and
 393 injection rates of six stages (blue line) are compared against induced earthquake magnitudes (circles).
 394 b) Locations of six stages (diamonds; HF1-HF6), along the well bore (black line), and the resultant
 395 earthquakes (circles). Injection stages and corresponding earthquakes are colour coordinated in all
 396 panels.
 397
 398

399 3.1.2 CAP-tests results at the Äspö HRL

400 To begin assessing if some process might be restricting magnitude growth at the Äspö
 401 HRL, we fit the GR-MFD to the catalogue data from each injection stage (*i.e.*, HF1-HF6). To

402 account for magnitude errors, we employ a 50-trial bootstrap process in which the catalogue
 403 magnitudes are dithered by ± 0.1 (this includes a dithered M_c). Only four of the stages (HF1-
 404 HF3, & HF6) have enough data to examine. Overall, the earthquakes here appear to be
 405 deficient in large-magnitude events (Figure 5). Correspondingly, the δM_{LRG} discrepancies
 406 range between -0.2 to -0.4 for all stages. Assuming an unbound catalogue, these degrees-of-
 407 truncation (δM_{LRG}) would be $<1^{st}$, 3^{rd} , $<1^{st}$, and 6^{th} percentile events, respectively. These initial
 408 assessments are suggestive of some M_{MAX} upper bound restricting catalogue growth at the
 409 Äspö HRL.

410

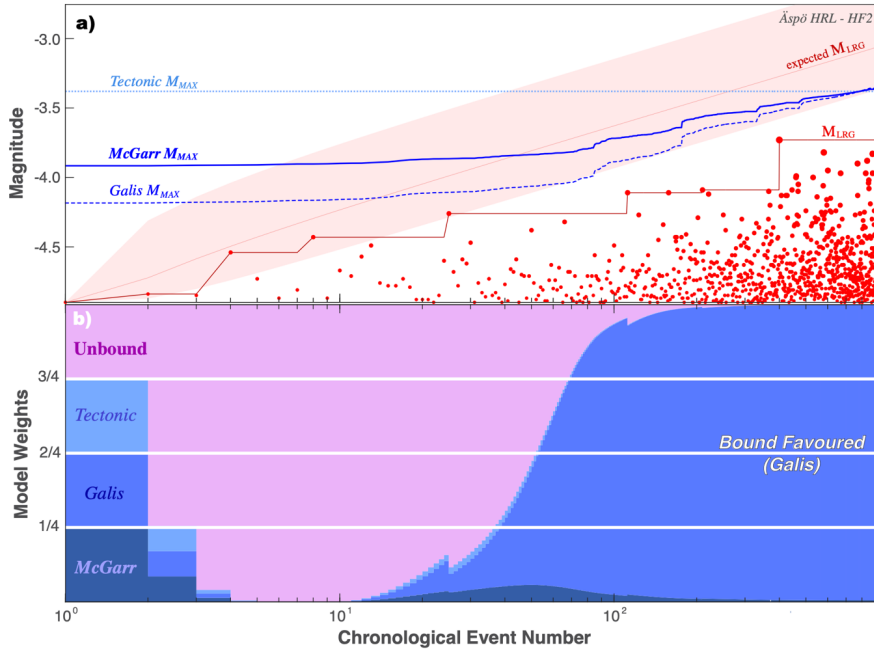


411

412 **Figure 5. Simple magnitude statistics for the Äspö HRL.** GR-MFD of cumulative events (circles),
 413 alongside best fit to the data (solid lines) and the magnitude-of-completeness (dashed line). Data is
 414 colour coordinated according to injection stages (*i.e.*, HF1-HF6).
 415

416 Next, we use the CAP-tests to detect and assess the potential for M_{MAX} more rigorously.
 417 The KS-test is performed 50 times, in which the catalogue magnitudes are dithered (including
 418 a dithered truncation magnitude). The KS-test also performs 100 reshuffles within each trial.
 419 Average KS-test confidences are $>99.99\%$, $>99.99\%$, 99.87% , and 68.85% for stages HF1-
 420 HF3 and HF6, respectively. We perform 50 MLE-tests using dithered catalogues and 100
 421 reshuffles within each trial. Similarly, MLE-tests suggest the standard error in fitted M_{MAX}
 422 values is 0.02, <0.01 , 0.02, and 0.18 for stages HF1-HF3 and HF6, respectively. Next, we seek
 423 test hypotheses for the functional form of M_{MAX} : our EW-tests focus on McGarr-like (McGarr,
 424 2014; Hallo et al., 2014; Elsworth, et al., 2025), the Galis-like model (Galis et al., 2017), a
 425 constant tectonic upper bound (Kanamori & Anderson, 1975), and the unbound null hypothesis.
 426 Similarly, EW-tests also show evidence for an M_{MAX} bound process, most strongly evidenced
 427 with stage HF2 (Figures 6 & S1-S3). By the end of HF2 stimulation, the Galis-like model is
 428 >100 times more likely than the unbound model (Figure 6).

429



430

431 **Figure 6. Using the EW-test to discern between M_{MAX} models for HF2 at the Äspö HRL.** a) The
 432 chronological sequence of earthquake magnitudes (red circles), the observed M_{LRG} (red line), and the
 433 expected M_{LRG} at the 10/50/90 percentiles (red area) are compared against M_{MAX} hypotheses (blue
 434 lines). b) The corresponding ensemble weights update as new data is encountered.
 435

436 Last, we organize our results for all injection stages at the Äspö HRL – for convenience
 437 to the reader. These results are summarized below (Table 1).
 438

Case		Simple-tests		CAP-tests			Resolution			
UGL	Stage	b -value	δM_{LRG}	KS-test	MLE-test	EW-test	M_{MAX} model	$N \geq M_C$	M_{LRG}	M_C
Äspö HRL	HF2	1.71±0.08	-0.32	>99.99%	<0.01	>100	Galis	898	-3.48	-4.9
Äspö HRL	HF1	1.91±0.11	-0.41	>99.99%	0.02	~11	Tectonic	509	-3.89	-4.9
Äspö HRL	HF6	1.90±0.11	-0.24	68.85%	0.18	~0.3	Indeterminate	540	-3.69	-4.9
Äspö HRL	HF3	2.37±0.17	-0.36	99.87%	0.02	~1.3	Tectonic	265	-4.22	-4.9

439 **Table 1. Summary of results at the Äspö HRL.** All the prior results of our simple-tests and CAP-
 440 tests are compiled here for convenience. Additionally, we have coordinated individual entries
 441 according to their interpretation: blue for bound, pink for unbound, and uncoloured for indeterminate.
 442

443 3.1.3 Interpretations for the Äspö HRL

Deleted: Unbound

445 ~~All the stages at the Äspö HRL appear to have some evidence of a bound process~~
446 ~~restricting the growth of earthquake magnitudes. The most convincing of the cases is also the~~
447 ~~most well-resolved one: for HF2, all the simple/CAP-tests unanimously indicate a bound~~
448 ~~process with strong statistical significance. As the cases become less well-resolved, the~~
449 ~~statistical confidence also diminishes. For example, the HF1 and HF3 stages have most CAP-~~
450 ~~tests indicating a bound process, only the EW-test of HF3 narrowly falls short of statistical~~
451 ~~significance. The HF6 stage produces the most mixed results: simple-tests, MLE-test, and EW-~~
452 ~~test are indeterminate, while the KS-test is unbound. It is worthwhile to mention that HF6~~
453 ~~differed in stimulation approach in two ways: the first sub-stage of HF6 was the largest injected~~
454 ~~volume (with reduced volume for later sub-stages) and the last three sub-stages were performed~~
455 ~~on a different day.~~

Deleted: Overall,

Deleted: a

456 Overall, we interpret stage HF2 as certainly being bound. Stages HF1 and HF3 as likely
457 to be bound, but likely needing more well-resolved catalogues to better discern M_{MAX} . We
458 hesitate to make a clear statement for HF6, which appears indeterminate due to data limitations.

Formatted: Indent: First line: 1.27 cm

459 The interpretation that all the Äspö HRL stages were (likely) bound corresponds with
460 the geophysical interpretations from relevant studies. The intention of the Äspö HRL was to
461 test various stimulation programs against the complexity/growth of hydraulic fractures (Zang
462 et al., 2019; 2021). Stage intervals were chosen to avoid natural fractures, and impression
463 packers noted the generation of new hydraulic fractures (Zimmerman et al., 2019).
464 Furthermore, the progressive growth of the HF2 hydraulic fracture plane was inferred jointly
465 from the microseismic and deformation constraints (Niemz et al., 2020; 2021). In this sense,
466 a progressively growing fracture aligns well with the bound interpretation: the finite extent of
467 a fracture limits M_{MAX} via geometric considerations (Kanamori & Anderson, 1975). As
468 stimulation continues, the fracture continues to grow; thus, the value of M_{MAX} would increase
469 alongside the injected volume. Correspondingly, each of the Äspö stages indicated bound
470 growth (albeit with varying degrees of confidence).

471 These interpretations at the Äspö HRL constitute the simplest interpretation. We
472 describe a scenario as to how hydraulic fracturing would be linked to a bound M_{MAX}
473 interpretation. Regardless of the fracture network's complexity, the finite spatial extent of
474 stimulated fractures ultimately restricts magnitude growth.

475

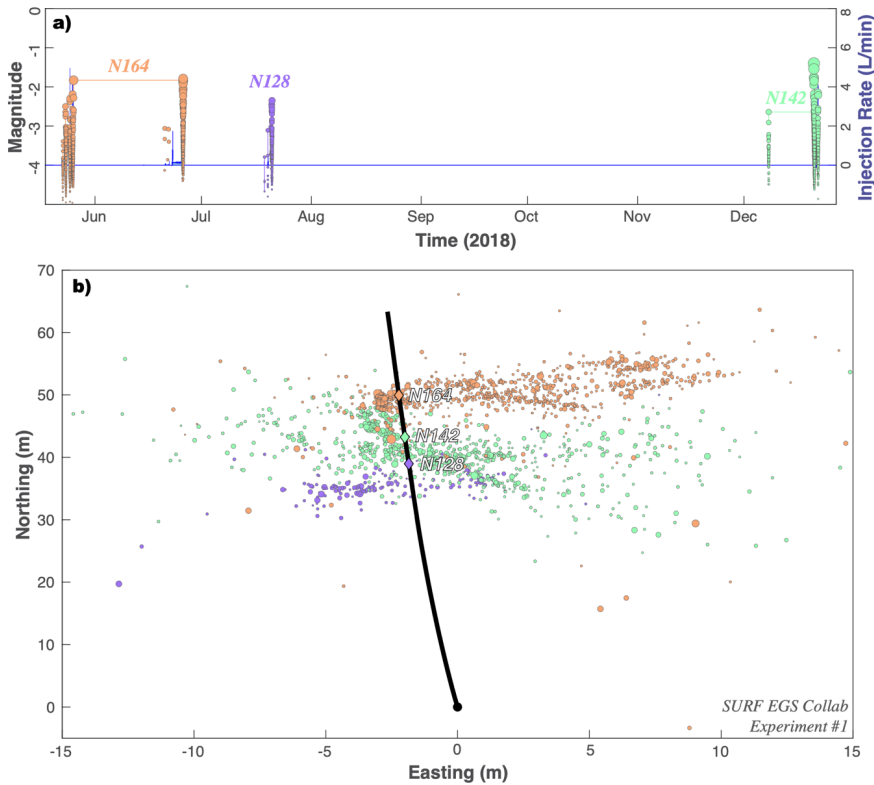
476 **3.2 The Sanford Underground Research Facility**

477 **3.2.1 Overview of the EGS Collab Experiment #1**

480 The SURF is located near Lead, South Dakota, and has repurposed the Homestake gold
481 mine (Figure 3). The SURF is a research facility operated by the South Dakota Science and
482 Technology Authority to study rare-process physics (Heise, 2015). The EGS Collab takes
483 advantage of the SURF, by using this facility to host hydraulic stimulation experiments at field-
484 scale depths of ~1.5 km (Dobson et al., 2018; Kneafsey et al., 2018; Morris et al., 2018).

485 The EGS Collab Experiment #1 intended to connect injection and production boreholes
486 via stimulated fractures in a controlled environment (Kneafsey et al., 2020; Morris et al., 2018).
487 Injection and production boreholes were drilled subparallel to the estimated minimum principal
488 stress direction (Oldenburg et al., 2017) in the phyllites of the Precambrian-aged Poorman
489 Formation (Kneafsey et al., 2020). These metamorphic rocks are strongly foliated and highly
490 anisotropic (Frash et al., 2019; Vigilante et al., 2017). The rock mass is generally thought to
491 be low permeability ($\sim 10^{-18}$ m²), with a thermally altered stress field (Singh et al., 2019). Some
492 natural fractures were noted in borehole cores (Fu et al., 2021), with at least one noteworthy
493 fracture that is naturally/actively flowing (Wu et al., 2021a). Starting in May 2018, stimulation
494 stages took place at three wellbore intervals (N164, N142, N128), covering both hydraulic
495 stimulation and hydraulic characterization programs; stimulation programs injected on the
496 order of 10s L of water per interval (Morris et al., 2018; White et al., 2019). Resulting
497 microseismicity was recorded for each interval, with ~2,000 located events (Schoenball et al.,
498 2019; 2020; Chai et al., 2020; Qin et al., 2024). Studies have covered topics including
499 modeling heat transport (Wu et al., 2021b), strain/deformation (Guglielmi et al., 2021), and
500 hydraulic fracture propagation (Li & Zhang, 2023). Data for the EGS Collab Experiment #1
501 is publicly available (<https://gdr.openei.org/>) and a spatiotemporal summary of stimulation
502 events is plotted (Figure 7).

503



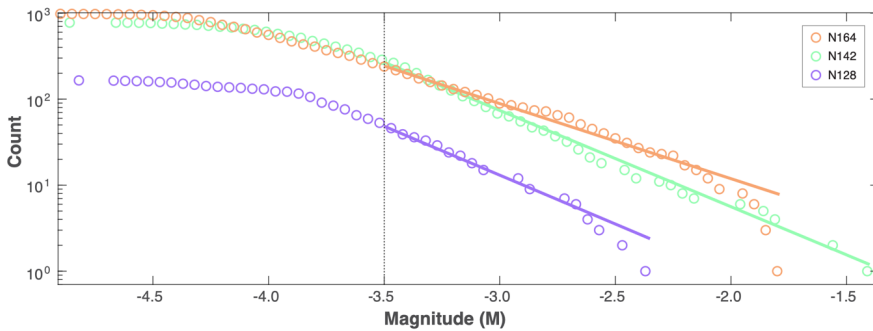
504

505 **Figure 7. Hydraulic stimulation and earthquake response for SURF Experiment #1.** a) Timings
 506 and injection rates of three stages (blue line) are compared against induced earthquake magnitudes
 507 (circles). b) Locations of three stages (diamonds; N164, N142, N128), along the well bore (black line),
 508 and the resultant earthquakes (circles). Injection stages and corresponding earthquakes are colour
 509 coordinated in all panels.
 510

511 3.2.2 CAP-tests results from the EGS Collab Experiment #1

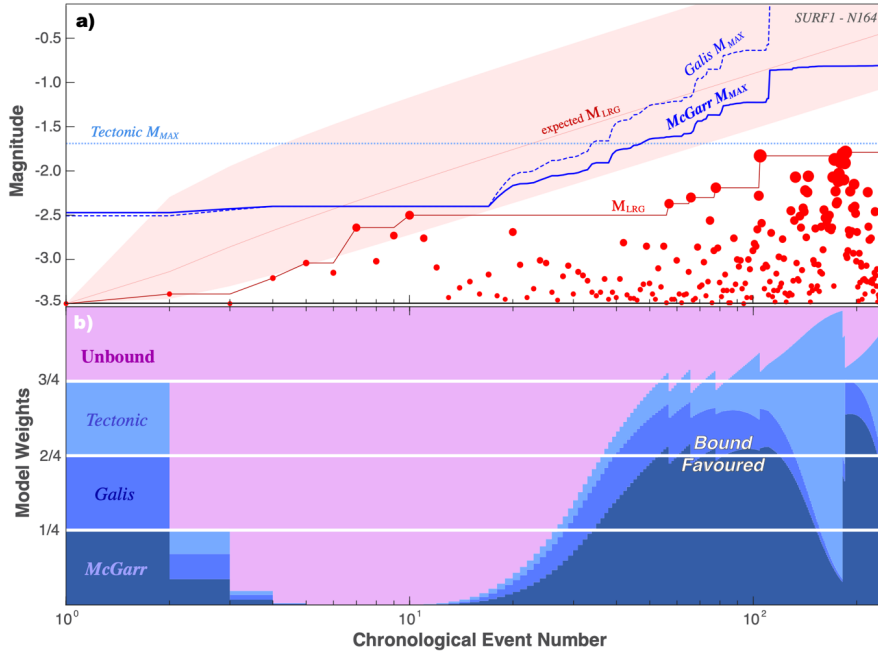
512 To begin assessing if some process might be restricting magnitude growth at SURF
 513 Experiment #1, we fit the GR-MFD to the catalogue data from each injection stage (*i.e.*, N164,
 514 N142, N128). To account for magnitude errors, we employ a 50-trial bootstrap process in
 515 which the catalogue magnitudes are dithered by ± 0.1 (this includes a dithered M_c). Only one
 516 of the stages (N164) appear to be appreciably deficient in large magnitude events (Figure 8).
 517 Correspondingly, the δM_{LRG} discrepancy is significant for N164 (-1.15 M), but fairly small for
 518 N142 (-0.05 M) and N128 (-0.28 M). Assuming an unbound catalogue, the δM_{LRG} discrepancy
 519 for N164 would be a $<1^{st}$ percentile event; stages N142 (10th percentile) and N128 (33rd

520 percentile) are more commonly expected occurrences. These initial assessments are suggestive
 521 of some M_{MAX} upper bound restricting catalogue growth for one stage at SURF Experiment
 522 #1.
 523



524 **Figure 8. Simple magnitude statistics for SURF Experiment #1.** GR-MFD of cumulative events
 525 (circles), alongside best fit to the data (solid lines) and the magnitude-of-completeness (dashed line).
 526 Data is colour coordinated according to injection stage (*i.e.*, N164, N142, N128).
 527
 528

529 Next, we use the CAP-tests to detect and assess the potential for M_{MAX} more rigorously.
 530 The KS-test is performed 50 times, in which the catalogue magnitudes are dithered (including
 531 a dithered truncation magnitude). The KS-test also performs 100 reshuffles within each trial.
 532 Again, KS-test results are split, with average confidences of 99.96% for stage N164, but
 533 34.23% and 74.39% for stages N142 and N128, respectively. We perform 50 MLE-tests using
 534 dithered catalogues and 100 reshuffles within each trial. MLE-tests are also split: standard
 535 error in fitted M_{MAX} values are 0.10, 2.18, and 1.31 for stages N164, N142, and N128,
 536 respectively. Similarly, EW-tests also shows suggestive evidence for an M_{MAX} bound process
 537 with N164 (Figure 9), but certainly not for stages N142 and N128 (Figures S4-S5).
 538



539
 540 **Figure 9. Using the EW-test to discern between M_{MAX} models for N164 for SURF Experiment #1.**
 541 a) The chronological sequence of earthquake magnitudes (red circles), the observed M_{LRG} (red line),
 542 and the expected M_{LRG} at the 10/50/90 percentiles (red area) are compared against M_{MAX} hypotheses
 543 (blue lines). b) The corresponding ensemble weights update as new data is encountered.
 544

545 Last, we organize our results for all injection stages at SURF Experiment #1 – for
 546 convenience to the reader. These results are summarized below (Table 2).
 547

Case		Simple-tests		CAP-tests			Resolution			
UGL	Stage	b -value	δM_{LRG}	KS-test	MLE-test	EW-test	M_{MAX} model	$N \geq M_C$	M_{LRG}	M_C
SURF #1	N164	0.83±0.02	-1.15	99.96%	0.10	~6.0	McGarr/Tectonic	239	-1.79	-3.5
SURF #1	N142	1.13±0.04	-0.06	34.23%	2.18	~0.11	Unbound	282	-1.40	-3.5
SURF #1	N128	1.18±0.05	-0.28	74.39%	1.31	~0.04	Unbound	50	-2.35	-3.5

548 **Table 2. Summary of results for the SURF EGS Collab Experiment #1.** All the prior results of our
 549 simple-tests and CAP-tests are compiled here for convenience. Additionally, we have coordinated
 550 individual entries according to their interpretation: blue for bound, pink for unbound, and uncoloured
 551 for indeterminate.
 552

553 3.2.3 Interpretations for the EGS Collab Experiment #1

554 CAP-test results at SURF Experiment #1 have similarities and differences from those
 555 at the Äspö HRL. For example, stage N164 is similar to the stages at the Äspö HRL: both

556 simple-tests and CAP-tests unanimously agree on an M_{MAX} bound – with varying degrees of
557 confidence. On the other hand, stages N142 and N128 differ in that they produce strong and
558 unambiguous unbound inferences. Because of this, we interpret stages N142 and N128 to be
559 truly unbound.

560 The interest in considering UGL cases is the wealth of complementary geophysical
561 information to cross-examine against the results of CAP-tests. The stimulation at stage N164
562 is predominantly understood to be the creation of a new fracture network. This interpretation
563 comes from multiple lines of evidence: the orientation of microseismic fault planes with respect
564 to the ambient stress field (Schoenball et al., 2020), deformation constraints on fracture motion
565 (Guglielmi et al., 2021), significant recovery of injected fluid (White et al., 2019), and direct
566 evidence of new fluid jets intersecting the producing well (Fu et al., 2021). The later N164
567 injections (*i.e.*, June 2018) were performed from the producing well side, into the newly created
568 fracture network. That said, some complexity in the N164 stimulation suggested limited
569 interaction with natural fractures, via either arrests or redirected continuation of fracture growth
570 (Schoenball et al., 2020; Fu et al., 2021). Overall, these inferences are consistent with finite
571 hydraulic fractures bounding the growth of earthquake magnitudes – which are the same
572 interpretations made for the Äspö HRL.

573 On the other hand, stages N142 and N128 had significant interactions with natural pre-
574 existing fractures, and likely reactivated them in shear rather than creating a new fracture
575 network. These inferences/interpretations come from the orientation of microseismic fault
576 planes with respect to the ambient stress field, corroboration with well image logs, and
577 observations of shear deformation (Schoenball et al., 2020). The connection to fractures/faults
578 allows for seemingly unbound magnitude growth, as the spatial extent of these pre-existing
579 structures have the potential to host larger events.

580 These interpretations at SURF Experiment #1 constitute the next level of complexity in
581 interpretation. We describe a scenario where hydraulic stimulation could interact with natural
582 fractures/faults to produce an unbound process. Said another way, the interaction with natural
583 fractures/faults (of sufficient size) can facilitate unbound magnitude growth.

584

585 **3.3 The Grimsel Test Site**

586 3.3.1 Overview of the GTS

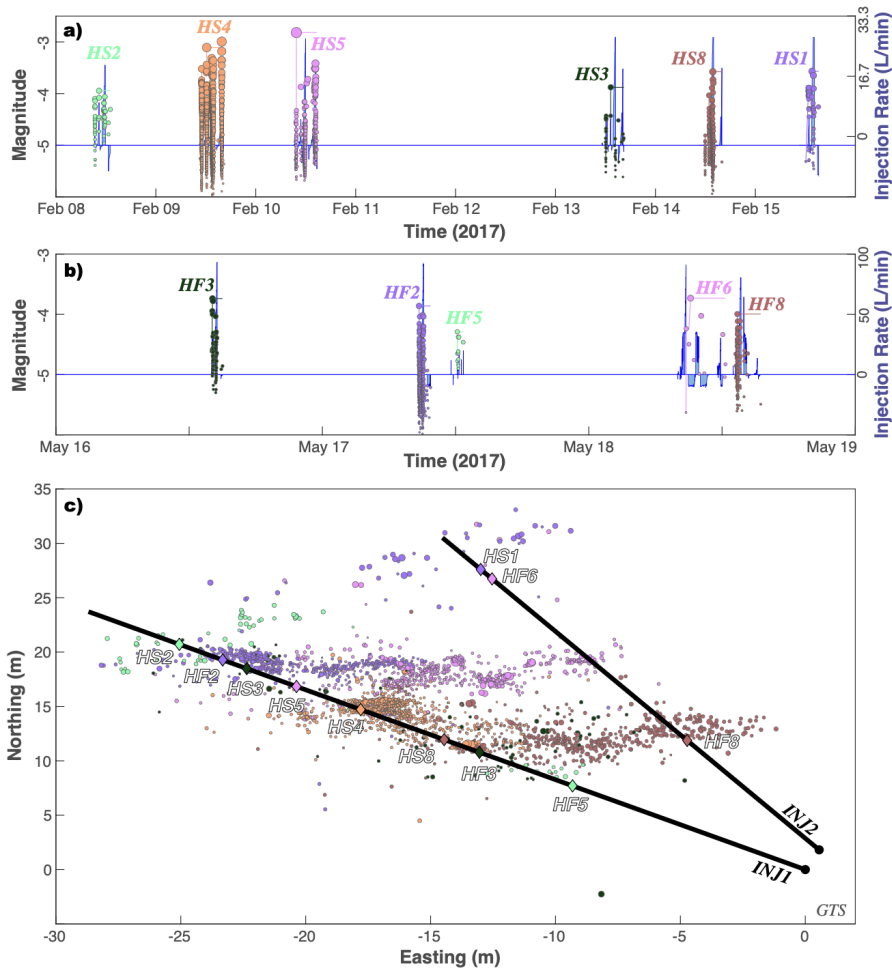
587 The GTS is located near the Grimsel pass in the central Swiss Alps (Figure 3), ~450 m
588 below the Juchlistock in the Varsican-aged Aar Massif granites (Schneeberger et al., 2019).
589 The GTS was established in 1984 as an underground research facility to study the safe disposal

590 of nuclear waste. It is owned and operated by the National Cooperation for Radioactive Waste
591 Disposal (Nagra; <https://www.grimsef.com/>).

592 The intention of recent (February-May 2017) injection experiments at the GTS was to
593 demonstrate the stimulation of fractures at the decameter scale and to better understand how to
594 manage induced seismicity (Gischig et al., 2016; Amann et al., 2018). Twelve injection stages
595 spanning ~1 m intervals were situated in two boreholes (~45 m long) (Gischig et al., 2020): six
596 related to stimulation via hydraulic fracturing (HF1-HF8) (Dutler et al., 2019) and six more via
597 hydroshearing (HS1-HS8) (Krietsch et al., 2020b). Each stage used (on the order of) ~1000 L
598 of injected fluid, spread between 4 injection sub-cycles. The role of natural faults and fractures
599 are a prominent focus of the GTS injection experiments, which injected into either brittle-
600 ductile shear zones, ductile shear zones, or intact rock (Doetsch et al., 2018a). The degree of
601 seismic response for individual stages was strongly heterogeneous in space, with stages HS4,
602 HS5, and HF2 being both the most seismically active and hosting the large events (M -3.0, M
603 -2.8 M, & M -3.9) (Villiger et al., 2020). Studies at the GTS were diverse, covering topics like
604 geological characterization (Krietsch et al., 2018a), stress inversion (Krietsch et al., 2019),
605 tomographic velocity changes (Doetsch et al., 2018b; Schopper et al., 2020), permeability
606 changes (Jalali et al., 2018; Brixel et al., 2020a; 2020b), and inferring fracture propagation
607 from hydromechanical response (Dutler et al., 2019; Krietsch et al., 2020a; 2020b). Data for
608 the GTS is publicly available (<https://doi.org/10.3929/ethz-b-000276170>) and a spatiotemporal
609 summary is plotted (Figure 10).

610

Deleted: AGRA

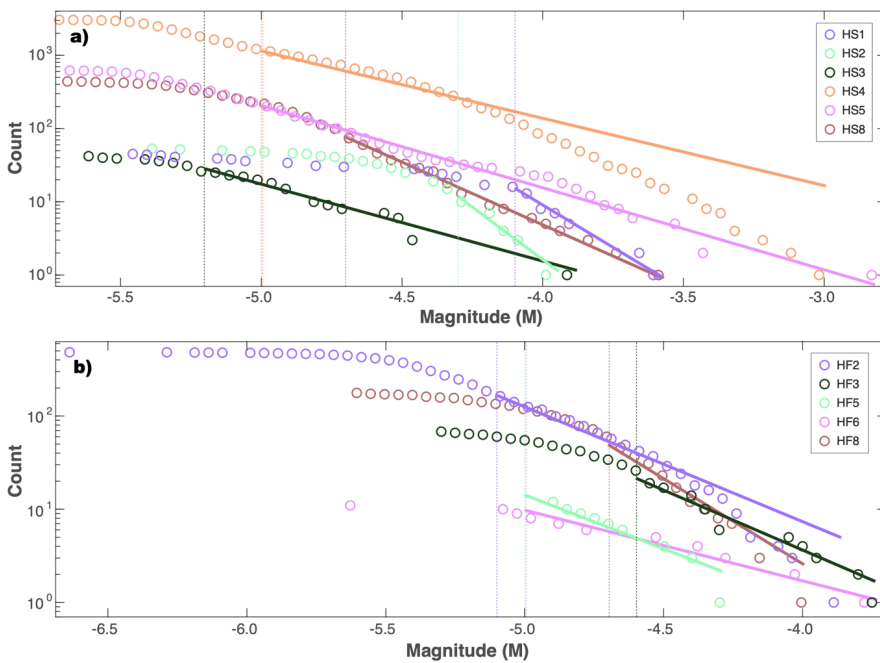


612
 613 **Figure 10. Hydraulic stimulation and earthquake response at the GTS.** a & b) Timings and
 614 injection rates of twelve stages (blue line) are compared against induced earthquake magnitudes
 615 (circles). c) Locations of twelve stages (diamonds; HFX & HSX), along the well bore (black line), and
 616 the resultant earthquakes (circles). Injection stages and corresponding earthquakes are colour
 617 coordinated in all panels.
 618

619 3.3.2 CAP-tests results at the GTS

620 To begin assessing if some process might be restricting magnitude growth at the GTS,
 621 we fit the GR-MFD to the catalogue data from each injection stage (*i.e.*, HSX & HFX). To
 622 account for magnitude errors, we employ a 50-trial bootstrap process in which the catalogue
 623 magnitudes are dithered by ± 0.1 (this includes a dithered M_c). Note that many of the stages

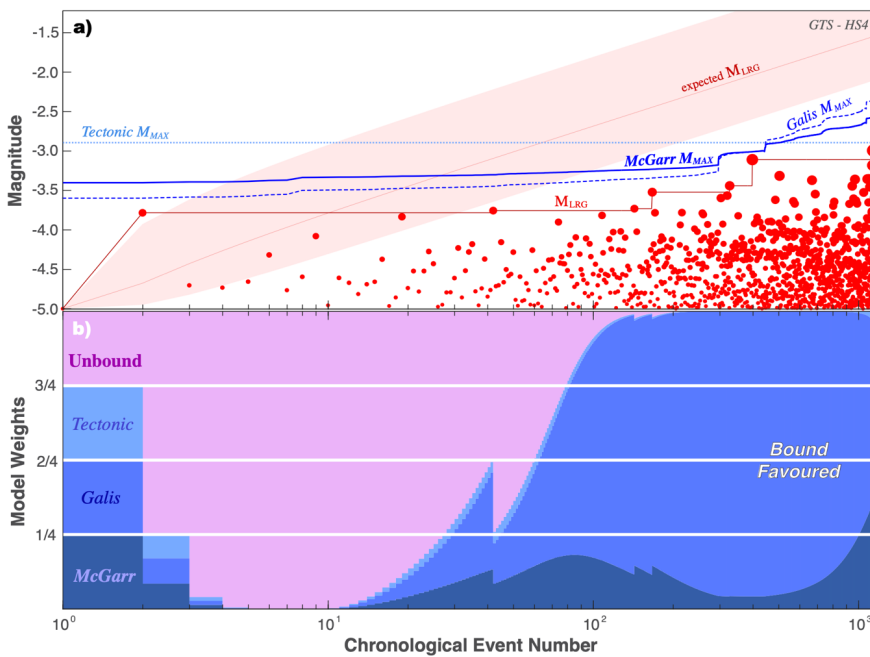
624 recorded here have too few events for a meaningful analysis; thus, we predominantly focus our
 625 discussions to a subset of stages. Only two of the stages (HS4 & HF2) appear to be appreciably
 626 deficient in large magnitude events (Figure 11). Correspondingly, the δM_{LRG} discrepancy is
 627 large for HS4 and HF2 (-1.31 M & -0.61 M), but fairly small for the other viable stages
 628 (between -0.19 and +0.08 M). Assuming an unbound catalogue, the δM_{LRG} discrepancy for
 629 HS4 and HF2 would both be $<1^{st}$ percentile events; all other stages are commonly expected
 630 occurrences. These initial assessments are suggestive of some M_{MAX} upper bound restricting
 631 catalogue growth for just two stages at the GTS.
 632



633
 634 **Figure 11. Simple magnitude statistics at the GTS.** GR-MFD of cumulative events (circles),
 635 alongside best fit to the data (solid lines) and the magnitude-of-completeness (dashed lines). Data is
 636 colour coordinated according to injection stage (*i.e.*, HSX & HFX) and separated into hydroshearing
 637 (a; HSX) or hydrofracturing experiments (b; HFX).
 638

639 Next, we use the CAP-tests to detect and assess the potential for M_{MAX} more rigorously.
 640 The KS-test is performed 50 times, in which the catalogue magnitudes are dithered (including
 641 a dithered truncation magnitude). The KS-test also performs 100 reshuffles within each trial.
 642 KS-test results are split, with strong confidences of $>99.99\%$ for stages HS4 & HF2, but

643 unconvincing values for all other stages. We perform 50 MLE-tests using dithered catalogues
 644 and 100 reshuffles within each trial. MLE-tests are also split: standard error in fitted M_{MAX}
 645 values are <0.01 and 0.02 for stages HS4 and HF2, but values are large (0.34 - 1.92) for all other
 646 stages. The EW-tests shows decisive evidence for an M_{MAX} bound process with HS4 (Figure
 647 12), and strong evidence for HF2 (Figure S6). All other stages have substantial-to-strong
 648 evidence for an unbound process via EW-tests (Figures S7-S10).
 649



650 **Figure 12. Using the EW-test to discern between M_{MAX} models for HS4 at the GTS.** a) The
 651 chronological sequence of earthquake magnitudes (red circles), the observed M_{LRG} (red line), and the
 652 expected M_{LRG} at the 10/50/90 percentiles (red area) are compared against M_{MAX} hypotheses (blue
 653 lines). b) The corresponding ensemble weights update as new data is encountered.
 654
 655

656 Last, we organize our results for all injection stages at the GTS – for convenience to
 657 the reader. These results are summarized below (Table 3).
 658

Case		Simple-tests		CAP-tests			Resolution			
UGL	Stage	b -value	δM_{LRG}	KS-test	MLE-test	EW-test	M_{MAX} model	$N \geq M_C$	M_{LRG}	M_C
GTS	HS4	0.93 ± 0.02	-1.31	>99.99%	<0.01	>100	Galis	1194	-3.00	-5.0
GTS	HS5	1.11 ± 0.05	+0.08	32.45%	0.76	~ 0.07	Unbound	214	-2.82	-5.0

GTS	HF2	1.20±0.05	-0.61	>99.99%	0.02	~60	Tectonic	170	-3.86	<u>-4.9</u>
GTS	HS8	1.68±0.11	-0.02	71.14%	1.34	~0.15	Unbound	81	-3.58	<u>-4.7</u>
GTS	HF8	1.97±0.14	-0.19	75.82%	0.34	~0.27	Unbound	58	-4.00	<u>-4.7</u>
GTS	HF3	1.55±0.10	-0.06	29.02%	1.92	~0.05	Unbound	26	-3.74	<u>-4.6</u>
GTS	HS3	1.05±0.05	-0.04	62.04%	0.98	~0.04	Unbound	26	-3.88	<u>-5.2</u>
GTS	HS1	2.40±0.22	+0.03	46.97%	1.26	~0.01	Unbound	15	-3.57	<u>-4.1</u>
GTS	HS2	2.76±0.38	-0.03	40.94%	0.81	~0.01	Unbound	11	-3.94	<u>-4.3</u>
GTS	HF5	1.16±0.05	-0.22	94.34%	2.23	~0.04	Unbound	12	-4.29	<u>-5.0</u>
GTS	HF6	0.73±0.06	-0.01	26.17%	3.61	~0.01	Unbound	9	-3.73	<u>-5.0</u>

659 **Table 3. Summary of results at the GTS.** All the prior results of our simple-tests and CAP-tests are
660 compiled here for convenience. Additionally, we have coordinated individual entries according to their
661 interpretation: blue for bound, pink for unbound, and uncoloured for indeterminate.
662

663 3.3.3 Interpretations for the GTS

664 In summary, most of the GTS stages appear to exhibit unbound growth of earthquake
665 magnitudes. Although, this interpretation varies in confidence, depending on the specific stage
666 in question, since many of the stages had relatively few events recorded. The most confidently
667 unbound case is HS5, which fails all of the simple-tests and CAP-tests. On the other hand,
668 there are two exceptions to this general trend: HS4 shows clear and definitive evidence for a
669 bound process, while HF2 shows strong evidence for a bound process. That said, stages with
670 fewer than 50 events are difficult to arrive at a clear interpretation between truly unbound or
671 simply lacking data.

672 The aims and scope of the GTS were to investigate the response of injection into
673 faults/fractures at the intermediate scale (Gischig et al., 2016; Amann et al., 2018). For
674 example, all HSX stages intentionally injected into previously known fractures of shear damage
675 zones (Krietsch et al., 2018); thus, micro-seismically delineated fault planes were generally
676 consistent with fracture/fault orientations (Villiger et al., 2020), near-field hydromechanical
677 effects were consistent with pre-existing fracture dislocation (Krietsch et al., 2020b), and many
678 stages were hydraulically connected to other boreholes via these stimulated fractures (Brixel et
679 al., 2020b). In particular to HS5, seismicity was well fit to a single fault plane (~16 m diameter)
680 oriented subparallel to the targeted fracture (Villiger et al., 2020), significant pressure increases
681 (~70-75% of injection pressure) were observed in boreholes 7-8 m away (Krietsch et al.,
682 2020a), likely due to transient permeability increases driven by fracture aperture changes
683 (Krietsch et al., 2020b). Furthermore, the diameter of the HS5 fault plane (~16 m) is
684 appreciably larger than the largest event diameter (~0.65 m), assuming a circular crack. HFX
685 stages started hydraulically fracturing intact rock and subsequently propagated/stimulated new
686 fractures (Dutler et al., 2019). However, the newly propagating fractures were inferred to have

687 significant interactions with pre-existing fractures, which served as pressure sinks that arrested
688 further growth (Dutler et al., 2019; Villiger et al., 2020). Note that HF6 is unique, since it
689 injected directly into a pre-existing fracture (by mistake) and thus can be considered a
690 hydroshearing experiment. Furthermore, the propagation of microseismic events along pipe-
691 like geometries was thought to be formed via the intersection with natural fractures (Dutler et
692 al., 2019). Given the prior interpretations of CAP-test results at SURF Experiment #1, we
693 would anticipate that all GTS stimulations should be unbound – because of their prominent
694 connection to pre-existing fractures. Bound cases would require special exceptions to this
695 generalization.

696 On the other hand, the HS4 stage is a clear exception to this generalization. The HS4
697 seismicity is not well-fit by a single plane. Instead, it is best fit by four intersecting planes (C1-
698 C4), where C1-C3 are oriented subparallel with pre-existing fractures and C4 is likely a new
699 tensile failure (Villiger et al., 2020; 2021). Clustering in focal mechanism slip style also
700 corresponds to spatial clusters (Villiger et al., 2021). Each cluster has seismicity spatially
701 restricted along discrete linear streaks (Villiger et al., 2021); these streaks grow/propagate
702 alongside injection, although their spatial extent (~1-2 m) is much smaller than other HSX fault
703 planes. In tectonic contexts, streaks are often interpreted as rheological boundaries between
704 seismic and creeping/locked fault segments (Rubin et al., 1999; Waldhauser et al., 2004). In
705 other hydraulic fracturing contexts, streaks have also been observed and analogously
706 interpreted (Rutledge et al., 2004; Evans et al., 2005). Thus, the streaks and clustering at HS4
707 have been interpreted as fractures channelizing fluid-flow towards highly seismogenic
708 asperities that slip perpendicular to the fluid migration direction (Villiger et al., 2021). In this
709 sense, we argue that HS4 seismicity is spatially bound to these asperities/streaks, giving rise to
710 the bound growth of magnitudes. Correspondingly, the GR-MFD for HS4 (Figure 11a) starts
711 to roll-off around M -4.3 and M -3.0 was the final M_{LRG} value; note that M -3.0 roughly
712 corresponds to a circular crack diameter of ~0.5-1.0 m, which is comparable to the spatial
713 extent of the streaks (~1-2 m).

714 Similarly, HF2 is also an exception to this generalization. The HF2 seismicity was best
715 fit by two intersecting planes, the first which resembles a newly created hydraulic fracture and
716 then a deflection to a more E-W orientation (Dutler et al., 2019; Villiger et al., 2020). It has
717 been suggested that this stage is exceptional in that it potentially has limited interaction with
718 pre-existing structures, being able to propagate fracture growth before leak-off into potential
719 fracture connections (Dutler et al., 2019; Villiger et al., 2020). In fact, the growing hydraulic
720 fracture intersected monitoring boreholes, reaching further than suggested by the microseismic

Deleted: s

722 events (Dutler et al., 2019). In this sense, we would argue that HF2 is most similar to the N164
723 stage at SURF Experiment #1. Correspondingly, both HF2 and N164 express a bound process
724 via CAP-tests.

725 These interpretations at the GTS constitute the greatest level of interpretive complexity
726 we will consider in this study. We have reiterated scenarios where hydraulic stimulation could
727 interact with natural fractures/faults to produce an unbound process. Regardless of the
728 stimulation program, the interaction with natural fractures/faults (of sufficient size) can
729 facilitate unbound magnitude growth. Exceptions come in the form of hydraulic fracturing
730 with limited interactions to natural fractures (HF2) and shear reactivation with seismicity
731 limited to streaks/asperities (HS4).

732

733 **4. Discussion**

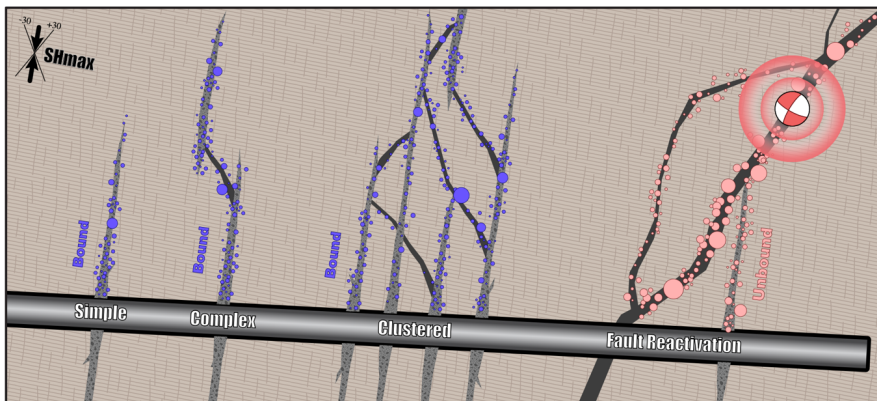
734 **4.1 Consolidating M_{MAX} interpretations**

735 In this sub-section, we synthesize the results and interpretations of this study in
736 comparison with relevant literature. We begin to jointly interpret the physical rationale behind
737 bound/unbound earthquake sequences. We start by reiterating the interpretations of CAP-tests
738 results at the UGLs and then discuss the correspondence with CAP-tests at the field-scale.

739 In the simplest case of the Äspö HRL (Section 3.1), stages were stimulated among intact
740 rock, creating new hydraulic pathways via stimulated fractures. The finite geometric extent of
741 these stimulated fractures limits the size of the largest events that can occur, at any given instant
742 (Figure 13). Although, the spatial extent of this fracture-bound M_{MAX} will change with
743 time/injection. Correspondingly, all Äspö HRL cases indicated a bound M_{MAX} process via
744 CAP-tests. While newly stimulated fractures were the intention of the Äspö HRL, bound cases
745 were also observed for analogous stages at SURF Experiment #1 (N164; Section 3.2) and the
746 GTS (HF2; Section 3.3), despite their different experiment objectives.

747 On the other hand, stages encountering more complicated interactions with pre-existing
748 fractures/faults tended to exhibit an unbound catalogue. For example, the simplest case of
749 fracture interaction was noted at SURF Experiment #1 (Section 3.2): the two stages (N142 &
750 N128) that intersected a natural fracture were also unbound via CAP-tests. Furthermore,
751 injection into faults/fractures was an aim of the GTS (Section 3.3), and these stages
752 predominantly exhibited an unbound process. We interpret this correspondence via
753 geometrical considerations again (Figure 13): an immediate hydraulic connection to a relatively
754 large-scale fracture system provides an opportunity for (apparently) unrestricted magnitude

755 growth. While we have not observed it at these three UGLs (to our knowledge), interactions
756 with smaller-scale pre-existing fractures would be expected to produce a bound sequence.
757



758
759 **Figure 13. Interactions between stimulated fractures and reactivated faults during hydraulic**
760 **fracturing.** A series of stages of increasing complexity (text labels) are considered alongside a
761 hypothetical well (black & grey rectangle). In the simple case, the host rock is split in tension via
762 stimulated fractures (grey polygons). In the complex case, small pre-existing faults (black polygons)
763 can also be reactivated in shear slip. The clustered case hydraulically connects a series of
764 stages/perforations into a single fracture/fault network. In the last case, stimulated fractures intersect a
765 large fault system that is critically-stressed for slip. By watching the growth of earthquake magnitudes,
766 CAP-tests can discern between bound cases (blue circles) and unbound cases (pink circles).
767

768 It is worth emphasizing that stage HS4 at the GTS is exceptional (Section 3.3), in that
769 a bound M_{MAX} process was observed for a case with strong natural fracture interactions. Thus,
770 this stage is an outlier to the general interpretive theme regarding natural faults/fractures. That
771 said, there is also good evidence for an alternative bounding mechanism at HS4. Earthquakes
772 were restricted to smaller streaks along larger fault plane trends (Villiger et al., 2021); these
773 streaks grew in spatial extent with increased injection volume. Streaks are interpreted as fault
774 heterogeneity, where seismic asperities are surrounded by a broader creeping/locked fault
775 segment (Rubin et al., 1999; Waldhauser et al., 2004; Rutledge et al., 2004; Evans et al., 2005).
776 Furthermore, the spatial extent of these streaks is comparable to the fault plane area of the
777 largest events observed. In this sense, HS4 seismicity is likely bound to these asperities/streaks,
778 giving rise to the bound growth of magnitudes. Following this logic, it should be possible to
779 test seismic asperities for a bound M_{MAX} process (via CAP-tests) in tectonic settings too.

780 A recent study performed CAP-tests on field-scale experiments (Schultz et al., 2025),
781 including both shale gas hydraulic fracturing at Preston New Road in the UK (Clarke et al.,

782 2019; Kettlety et al., 2021) and the enhanced geothermal system at Utah FORGE (Moore et
783 al., 2019; Niemez et al., 2025). CAP-tests indicated that many clustered stages followed a bound
784 process, while the more hazardous stages were unbound. Interpretations in these field-scale
785 cases followed a similar interpretation to UGL stages in this study (Section 4.1.1), albeit with
786 larger uncertainties. This interpretation was partly driven by clustering sensitivity tests that
787 showed omitting/ignoring earlier bound stages tended to diminish statistical confidence
788 (Schultz et al., 2025) – providing an inference to the importance of accurate clustering and
789 hydraulic connectivity for bound sequences. Certainly, natural fractures have demonstrably
790 influenced the propagation of stimulated fractures (Jin et al., 2024). In this sense, the
791 verification of this interpretation at UGLs provides a potential conceptual linkage to the field-
792 scale, given their observational similarities. Prior results for bound processes are consistent
793 with stimulating a fracture system with a restricted extent, while unbound cases likely have
794 reactivated larger fault systems (Schultz, 2024).

795

796 ***4.3 Empirically constraining the functional form of M_{MAX} vs V***

797 Up to this point, our study has focused on discerning between bound/unbound
798 sequences – and establishing the importance of natural fault/fracture systems within this
799 dichotomy. However, our discussion has neglected the underlying physical mechanisms
800 responsible for creating this bound M_{MAX} process. Here, we further discuss the underlying
801 physical mechanisms, for all the known bound sequences with data available (Figure 3) – both
802 in this study and past studies (Schultz et al., 2025).

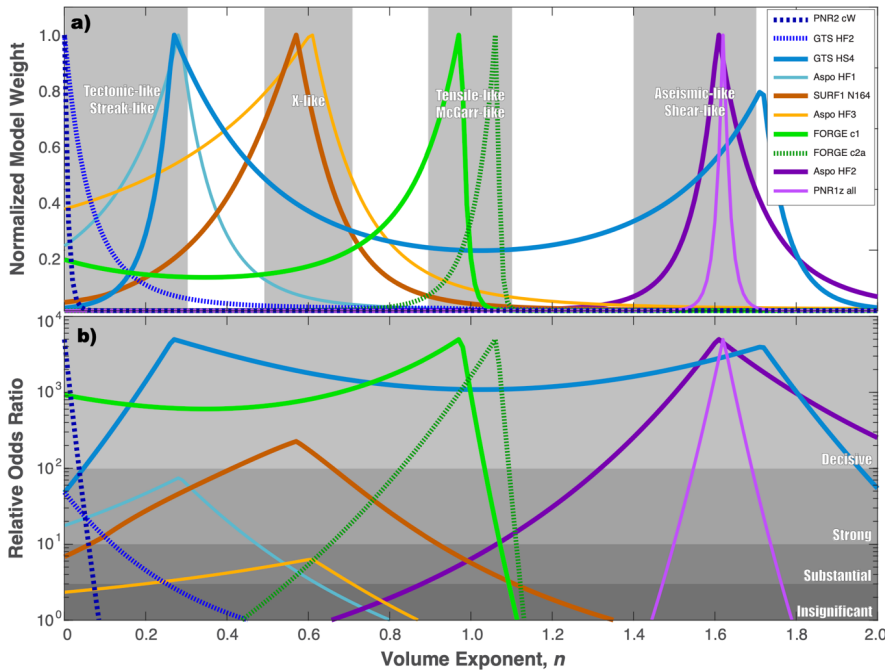
803 Numerous theoretical models of M_{MAX} and fracture propagation have been proposed in
804 the literature (Eaton & Igonin, 2018). The simplest model considers a physical limitation based
805 on the geometry of the finite fault extent (Kanamori & Anderson, 1975); For a circular fault
806 with radius R and constant stress drop $\Delta\sigma$, the seismic moment release is given via the equation
807 $M_0 = \frac{16}{7} \Delta\sigma R^3$. Seismic moment can then be translated into an M_{MAX} magnitude via the
808 moment magnitude relationship (Hanks & Kanamori, 1979). Non-stationary M_{MAX} models
809 have been proposed for induced seismicity based on the footprint of stress perturbation along
810 a fault (Shapiro et al., 2011), the evolution of seismic moment (McGarr, 2014; Hallo et al.,
811 2014; Elsworth et al., 2025), self-arrested rupture dynamics (Galis et al., 2017), or time-
812 dependent pressure diffusion (Shapiro et al., 2021). Additionally, we can consider the finite
813 extent of fracture propagation via an aseismic shear crack (Danré et al., 2024) or a tensile crack
814 (Davis et al., 2020). These two models suggest time-varying fracture radii based on the

815 equations $R(t) = \sqrt{s_d V(t)}$ and $R(t) = \sqrt[3]{k V(t)}$, respectively. [Here, \$s_d\$ and \$k\$ are injection](#)
816 [propagation coefficients.](#) M_{MAX} models have been investigated in numerous prior studies
817 (Kwiatek et al., 2018; Li et al., 2021; Yu et al., 2024; Langenbruch et al., 2024; Lanza et al.,
818 2026).

819 Examining the theoretical models illustrates a common mathematical theme: seismic
820 moment release (M_0) is proportional to injected volume, raised to some exponent. For example,
821 the McGarr-like model considers $M_0 \propto V^1$ (McGarr, 2014), while the Galis-like model
822 considers $M_0 \propto V^{3/2}$ (Galis et al., 2017). Similarly, a growing tensile crack is equivalent to M_0
823 $\propto V^1$ (Kanamori & Anderson, 1975; Davis et al., 2020), while a growing aseismic shear crack
824 is $M_0 \propto V^{3/2}$ (Kanamori & Anderson, 1975; Danré et al., 2024; Im & Avouac, 2025; Sáez et
825 al., 2025). Even purely tectonic/geometric limitations can be cast into this form as $M_0 \propto V^0$.
826 Given this commonality, we consider a generic family of M_{MAX} models that have a functional
827 form of $M_{MAX} \propto \log_{10}(V^n)$. This generalization is advantageous, as the EW-test can consider
828 any arbitrary M_{MAX} function. Following this logic, we use these arbitrary functions within the
829 EW-test to find the best-fitting n -exponent for each bound case. To ensure a fair comparison,
830 each competing/candidate M_{MAX} model is first fit to the case data before the EW-test selects
831 the best model.

832 This investigation indicates that the underlying physical mechanisms are varied among
833 cases (Figure 14). However, the results tend to aggregate into four distinct categories:
834 geometric/streak-like (n 0.0-0.3), X-like (n 0.5-0.7), McGarr/tensile-like (n 0.9-1.1), and
835 aseismic/shear-like (n 1.4-1.7). Bounding mechanisms can be varied, even between similar
836 stages (e.g., Äspö HRL, HF1-HF3). Higher n -exponents tend to be less confident, likely
837 because aseismic/shear-like exponents emulate/approach unbound-like magnitude growth (van
838 der Elst et al., 2016; Galis et al., 2017). Other geophysical data/studies to corroborate the
839 inferences of physical mechanisms are generally limited to a few cases. For example, the
840 propagation of microseismic events at Utah FORGE stages 1-3 were best-fit by tensile-like
841 models (Clarkson et al., 2025; Lanza et al., 2026; [Niemz et al., 2026](#)), which independently
842 corresponds to our best-fit n -exponents (0.97 & 1.06) for clusters 1 ([stages 1-2](#)) and 2 ([stages](#)
843 [3-6](#)) (Figure 14), [as defined in Schultz et al. \(2025\)](#). Interestingly, the low n -exponent
844 associated with HS4 at the GTS is consistent with the observation of tectonic streaks/asperities
845 that exhibited limited spatial growth during injection (Villiger et al., 2021). The X-like
846 category is exceptional, since there is (to our knowledge) no previously suggested model for
847 this n -exponent. This could be potentially explained by M_{MAX} models that do not fit the V^n

848 generalization (Shapiro et al., 2011; 2021), an as-of-yet undiscovered M_{MAX} model, or
 849 observational biases for encountering a relatively large pre-existing fracture network (V^0) that
 850 also starts growing alongside injection (V^1 or $V^{3/2}$). Currently, we favour the observational
 851 bias interpretation for the X-like category, based on the results of drop-out tests that
 852 demonstrate how an intermediate sized pre-existing fracture network that also grows alongside
 853 injection can produce a mixed n -exponent with poorly-resolved data (Supplementary Section
 854 S1 & Figure S16). We consider it likely that these considerations were a factor for the SURE
 855 N164 and Äspö HF3 cases, which indicated the next closest M_{MAX} model when restricting
 856 choices to our three bound options (Tables 1 & 2). Accounting for some prior growth appears
 857 to be an important consideration for discerning the true M_{MAX} model.



858
 859 **Figure 14. Searching for volume-exponents.** The EW-test fit to case data (lines) for both a)
 860 normalized model weights and b) odds ratios (relative to the unbound null hypothesis). Strength of
 861 statistical confidence and n -exponent categories are shown with grey shaded areas (and text callouts).
 862 Note that relative odds ratios are capped at 5000 to facilitate easier comparison via plotting.
 863

864 Additional UGL study alongside refinements to CAP-tests (potentially also considering
 865 other candidate M_{MAX} models) will likely shed light on the physical processes underlying
 866 bound sequences. For example, CAP-tests could be used to systematically search for M_{MAX}

867 models in other datasets. We note that this approach could be straightforwardly adapted to
 868 forecast the ‘next largest event’ (Cao et al., 2020), using these weights as part of either a logic-
 869 tree (Bommer & Verdon, 2024) or an ensemble of models (Schultz et al., 2023c).

870

871 **4.3 Exceptions to bound/unbound interpretations**

872 Thus far, we have predominantly interpreted the difference between bound/unbound
 873 sequences via distinctions between fracture stimulation and fault reactivation (Figure 13).
 874 While this appears to capture the first-order effects, there likely exists subtleties that can deviate
 875 from this conjecture.

876

877 4.3.1 Exceptions to the bound-fracture interpretation

878 We have predominantly interpreted bound sequences arising from the finite (and
 879 time/volume dependent) extent of a propagating fracture restricting available slip area. While
 880 this interpretation matches both expectation and observation, we can still envision a scenario
 881 in which a finite fracture could produce an unbound sequence. For example, in the case that
 882 the finite extent of the fracture grows faster than the equivalent area of an unbound M_{LRG} . In
 883 this sense, while the sequence is technically bound, it would never be empirically inferable by
 884 magnitude information. Criteria for this condition are given below: for the V^n generalization
 885 of M_{MAX} as well as the tensile-like and shear-like fractures. There, the expected M_{LRG}
 886 formulation is a combination of the population expectation (van der Elst et al., 2016) coupled
 887 with a proportionality between injected volume and event counts (Shapiro et al., 2010). Note
 888 that Σ is the seismogenic index, a parameter indicating a fault’s potential to induce earthquakes
 889 per unit of injected fluid volume (Shapiro et al., 2010).

890
$$\left(\frac{2n}{3} - \frac{1}{b}\right) \log_{10}(V(t)) + \left(\frac{2}{3}\right) \log_{10}(c) - 9.1 \gg \frac{\Sigma}{b} \text{ (} V^n \text{ generalization)}$$

891
$$\left(1 - \frac{1}{b}\right) \log_{10}(V(t)) + \left(\frac{2}{3}\right) \log_{10}\left(\frac{16}{7} \Delta\sigma s_d^{3/2}\right) - 9.1 \gg \frac{\Sigma}{b} \text{ (tensile fracture)}$$

892
$$\left(\frac{2}{3} - \frac{1}{b}\right) \log_{10}(V(t)) + \left(\frac{2}{3}\right) \log_{10}\left(\frac{16}{7} \Delta\sigma k\right) - 9.1 \gg \frac{\Sigma}{b} \text{ (Shear fracture)}$$

893 As a reminder of terms: $V(t)$ is the injection volume time-series, n is the volume exponent, b
 894 is the b -value, $\Delta\sigma$ is the stress drop, while c , s_d and k are injection propagation coefficients
 895 for different growth.

896

897 4.3.2 Exceptions to the unbound-fault interpretation

898 We have predominantly interpreted unbound sequences arising from fractures
899 interacting with relatively-large pre-existing faults. While this matches our expectation and
900 observations, we can still envision scenarios where pre-existing faults could produce bound
901 sequences. For example, M_{LRG} could be limited by the pre-existing faults being too small, the
902 *in situ* stress resolved on the fault (Gischig, 2015; Norbeck & Horne, 2018), time-dependence
903 of stress perturbations (Segall & Lu, 2015), fault geometry/complexity (Lee et al., 2024), fault
904 roughness (Mauer et al., 2020; Wang et al., 2024), material/stress heterogeneity (Kroll &
905 Cochran, 2021), rheology, or the extent of asperities. In fact, HS4 at the GTS is one such
906 exception: where streaks outlined the rheological boundary between seismic, asperities hosted
907 within an aseismic fault. If these factors are limiting M_{LRG} , CAP-tests should be able to discern
908 their effects.

Deleted: ally

910 5. Conclusions

911 In summary, we have rigorously tested CAP-tests against data from controlled injection
912 experiments at three underground laboratories. Bound sequences are consistent with
913 observations of new hydraulic fracturing growth, while unbound typically reactivate larger pre-
914 existing structures. Furthermore, the EW-test appears to be able aggregate generalized M_{MAX}
915 functions into categories consistent with theoretical considerations for tectonic/geometric
916 limits, tensile/McGarr-like growth, or aseismic/shear-like growth. This process is potentially
917 able to identify the underlying physical mechanism responsible for M_{MAX} , specific to an
918 individual earthquake sequence. Overall, the ability to robustly identify and constrain M_{MAX}
919 will likely be important for both induced seismicity and natural/tectonic earthquake sequences.

921 Acknowledgments

922 We would like to thank Luigi Passarelli for insightful conversations that helped the
923 interpretation of this study. We also thank Peter Niemz and an anonymous reviewer, whose
924 comments helped to improve this manuscript. We are grateful for the high-quality UGL studies
925 that facilitated our CAP-test interpretations, which would have been impossible otherwise.
926 This work is supported by the Seismogenic Fault Injection Test (SFIT), which is funded by the
927 Swiss National Science Foundation, under project number TMPFP2_224393. This work is
928 also supported by the CETPartnership, which is funded by the Clean Energy Transition
929 Partnership under the 2023 joint call for research proposals, co-funded by the European
930 Commission (GA N°101069750) and with the funding organizations detailed on
931 <https://cetpartnership.eu/funding-agencies-and-call-modules>.

933

934

935 **Data Availability**

936 The codes (and data) used to derive our results are available online at GitHub (**LINK**).

937 The catalogue and hydraulic datasets are also available online, from their source: for the Äspö

938 HRL (Zang et al., 2024), SURF EGS Collab Experiment #1 (<https://gdr.openei.org/>), and the

939 GTS (<https://doi.org/10.3929/ethz-b-000276170>).

940

941 **Author Contributions**

942 R.S. created the CAP-tests, gathered the data, analysed the cases, and wrote the manuscript.

943 L.V., and V.G. were involved in the curation of GTS catalogue and interpretation of the results.

944 S.W. provided project management. All authors were involved in manuscript editing and

945 review.

946

947 **Competing Interests**

948 The authors declare no competing interests.

949

950

951 **References**

952

953 Akaike, H. (1998). Information theory and an extension of the maximum likelihood principle.
954 In *Selected papers of hirotugu akaike* (pp. 199-213). New York, NY: Springer New York.

955

956 Amann, F., Gischig, V., Evans, K., Doetsch, J., Jalali, R., Valley, B., ... & Giardini, D.

957 (2018). The seismo-hydromechanical behavior during deep geothermal reservoir

958 stimulations: open questions tackled in a decameter-scale in situ stimulation experiment.

959 *Solid Earth*, 9(1), 115-137, <https://doi.org/10.5194/se-9-115-2018>.

960

961 Atkinson, G. M., Eaton, D. W., Ghofrani, H., Walker, D., Cheadle, B., Schultz, R., ... & Kao,

962 H. (2016). Hydraulic Fracturing and Seismicity in the Western Canada Sedimentary Basin.

963 *Seismological Research Letters*, 87(3), 631-647, <https://doi.org/10.1785/0220150263>.

964

965 Berger, V. W., & Zhou, Y. (2014). Kolmogorov–Smirnov test: Overview. *Wiley statsref:*

966 *Statistics reference online*, <https://doi.org/10.1002/9781118445112.stat06558>.

967

968 Bommer, J. J., Oates, S., Cepeda, J. M., Lindholm, C., Bird, J., Torres, R., ... & Rivas, J.

969 (2006). Control of hazard due to seismicity induced by a hot fractured rock geothermal

970 project. *Engineering Geology*, 83(4), 287-306, <https://doi.org/10.1016/j.enggeo.2005.11.002>.

971

972 Bommer, J. J. (2022). Earthquake hazard and risk analysis for natural and induced seismicity:

973 towards objective assessments in the face of uncertainty. *Bulletin of Earthquake Engineering*,

974 20(6), 2825-3069, <https://doi.org/10.1007/s10518-022-01357-4>.

975

976 Bommer, J., & Verdon, J. P. (2024). The maximum magnitude of natural and induced

977 earthquakes. *Geomechanics and Geophysics for Geo-Energy and Geo-Resources*, 10, 172,

978 <https://doi.org/10.1007/s40948-024-00895-2>.

979

980 Brixel, B., Klepikova, M., Jalali, M. R., Lei, Q., Roques, C., Kriestch, H., & Loew, S.

981 (2020a). Tracking fluid flow in shallow crustal fault zones: 1. Insights from single-hole

982 permeability estimates. *Journal of Geophysical Research: Solid Earth*, 125(4),

983 e2019JB018200, <https://doi.org/10.1029/2019JB018200>.

984

985 Brixel, B., Klepikova, M., Lei, Q., Roques, C., Jalali, M. R., Krietsch, H., & Loew, S.

986 (2020b). Tracking fluid flow in shallow crustal fault zones: 2. Insights from cross-hole forced

987 flow experiments in damage zones. *Journal of Geophysical Research: Solid Earth*, 125(4),

988 e2019JB019108, <https://doi.org/10.1029/2019JB019108>.

989

990 Cao, N. T., Eisner, L., & Jechumtálová, Z. (2020). Next record breaking magnitude for

991 injection induced seismicity. *First Break*, 38(2), 53-57, [https://doi.org/10.3997/1365-](https://doi.org/10.3997/1365-2397.fb2020010)

992 [2397.fb2020010](https://doi.org/10.3997/1365-2397.fb2020010).

993

994 Cao, N. T., Eisner, L., Jechumtálová, Z., Verdon, J., & Waheed, U. B. (2024). Upper limit

995 magnitudes for induced seismicity in energy industries. *Geophysical Prospecting*,

996 <https://doi.org/10.1111/1365-2478.13553>.

997

998 Chai, C., Maceira, M., Santos-Villalobos, H. J., Venkatakrishnan, S. V., Schoenball, M., Zhu,

999 W., ... & EGS Collab Team. (2020). Using a deep neural network and transfer learning to

1000 bridge scales for seismic phase picking. *Geophysical Research Letters*, 47(16),
1001 e2020GL088651, <https://doi.org/10.1029/2020GL088651>.
1002
1003 Clarke, H., Verdon, J. P., Kettlety, T., Baird, A. F., & Kendall, J. M. (2019). Real-time
1004 imaging, forecasting, and management of human-induced seismicity at Preston New Road,
1005 Lancashire, England. *Seismological Research Letters*, 90(5), 1902-1915,
1006 <https://doi.org/10.1785/0220190110>.
1007
1008 Clarkson, C.R., Alkhayyali W., & Zeinabady, D. (2025). Characterization and modeling of
1009 enhanced geothermal systems using methods developed for unconventional hydrocarbon
1010 reservoirs, *SPE Annual Technical Conference and Exhibition*, SPE-228230.
1011
1012 Danré, P., Garagash, D., De Barros, L., Cappa, F., & Ampuero, J. P. (2024). Control of
1013 seismicity migration in earthquake swarms by injected fluid volume and aseismic crack
1014 propagation. *Journal of Geophysical Research: Solid Earth*, 129(1), e2023JB027276,
1015 <https://doi.org/10.1029/2023JB027276>.
1016
1017 Davis, T., Rivalta, E., & Dahm, T. (2020). Critical fluid injection volumes for uncontrolled
1018 fracture ascent. *Geophysical Research Letters*, 47(14), e2020GL087774,
1019 <https://doi.org/10.1029/2020GL087774>.
1020
1021 DeDontney, N., Gans, C., Burnett, W., Burch, D., Garzon, J., Gist, G., ... & Younan, A.
1022 (2016). Maximum magnitude of induced earthquakes in the Groningen gas field. *ExxonMobil*
1023 *URC External Report*, [https://nam-onderzoeksrapporten.data-](https://nam-onderzoeksrapporten.data-app.nl/reports/download/groningen/en/36dea690-c7eb-4164-9d94-d9725381c426)
1024 [app.nl/reports/download/groningen/en/36dea690-c7eb-4164-9d94-d9725381c426](https://nam-onderzoeksrapporten.data-app.nl/reports/download/groningen/en/36dea690-c7eb-4164-9d94-d9725381c426).
1025
1026 Dobson, P., Kneafsey, T., Morris, J., Singh, A., Zoback, M., Roggenthen, W., ... & White, M.
1027 (2018). The EGS Collab hydroshear experiment at the Sanford Underground Research
1028 Facility—Siting criteria and evaluation of candidate sites. *Geothermal Resources Council*
1029 *Transactions*, 42, 708-723.
1030
1031 Doetsch, J., Gischig, V., Krietsch, H., Villiger, L., Amann, F., Dutler, N., Jalali, M., Brixel,
1032 B., Roques, C., Giertzuch, P., Kittilä, A., and Hochreutener, R. (2018a). Grimsel ISC
1033 Experimental Description, *ETH Zurich Report*, <https://doi.org/10.3929/ethz-b-000310581>.
1034
1035 Doetsch, J., Gischig, V. S., Villiger, L., Krietsch, H., Nejati, M., Amann, F., ... & Giardini, D.
1036 (2018b). Subsurface fluid pressure and rock deformation monitoring using seismic velocity
1037 observations. *Geophysical Research Letters*, 45(19), 10-389,
1038 <https://doi.org/10.1029/2018GL079009>.
1039
1040 Dorbath, L., Cuenot, N., Genter, A., & Frogneux, M. (2009). Seismic response of the
1041 fractured and faulted granite of Soultz-sous-Forêts (France) to 5 km deep massive water
1042 injections. *Geophysical Journal International*, 177(2), 653-675,
1043 <https://doi.org/10.1111/j.1365-246X.2009.04030.x>.
1044
1045 Dutler, N., Valley, B., Gischig, V., Villiger, L., Krietsch, H., Doetsch, J., ... & Amann, F.
1046 (2019). Hydraulic fracture propagation in a heterogeneous stress field in a crystalline rock
1047 mass. *Solid Earth*, 10(6), 1877-1904, <https://doi.org/10.5194/se-10-1877-2019>.
1048

1049 Eaton, D. W., & Igonin, N. (2018). What controls the maximum magnitude of injection-
1050 induced earthquakes?. *The Leading Edge*, 37(2), 135-140,
1051 <https://doi.org/10.1190/tle37020135.1>.
1052

1053 Elsworth, D., Li, Z., Yu, P., An, M., Zhang, F., Huang, R., ... & Liu, S. (2025). Constraints
1054 on triggered seismicity and its control on permeability evolution. *Journal of Rock Mechanics
and Geotechnical Engineering*, 17(1), 20-30, <https://doi.org/10.1016/j.jrmge.2024.11.035>.
1056

1057 Evans, K. F., Moriya, H., Niitsuma, H., Jones, R. H., Phillips, W. S., Genter, A., ... & Baria,
1058 R. (2005). Microseismicity and permeability enhancement of hydrogeologic structures during
1059 massive fluid injections into granite at 3 km depth at the Soultz HDR site. *Geophysical
Journal International*, 160(1), 388-412, <https://doi.org/10.1111/j.1365-246X.2004.02474.x>.
1061

1062 Foulger, G. R., Wilson, M. P., Gluyas, J. G., Julian, B. R., & Davies, R. J. (2018). Global
1063 review of human-induced earthquakes. *Earth-Science Reviews*, 178, 438-514,
1064 <https://doi.org/10.1016/j.earscirev.2017.07.008>.
1065

1066 Frash, L. P., Carey, J. W., & Welch, N. J. (2019, February). EGS collab experiment 1
1067 geomechanical and hydrological properties by triaxial direct shear. In *44th workshop on
1068 geothermal reservoir engineering*.
1069

1070 Fu, P., Schoenball, M., Ajo-Franklin, J. B., Chai, C., Maceira, M., Morris, J. P., ... & EGS
1071 Collab Team. (2021). Close observation of hydraulic fracturing at EGS Collab Experiment 1:
1072 Fracture trajectory, microseismic interpretations, and the role of natural fractures. *Journal of
1073 Geophysical Research: Solid Earth*, 126(7), e2020JB020840,
1074 <https://doi.org/10.1029/2020JB020840>.
1075

1076 Galis, M., Ampuero, J. P., Mai, P. M., & Cappa, F. (2017). Induced seismicity provides
1077 insight into why earthquake ruptures stop. *Science Advances*, 3(12), eaap7528,
1078 <https://doi.org/10.1126/sciadv.aap7528>.
1079

1080 Grigoli, F., Cesca, S., Rinaldi, A. P., Manconi, A., Lopez-Comino, J. A., Clinton, J. F., ... &
1081 Wiemer, S. (2018). The November 2017 Mw 5.5 Pohang earthquake: A possible case of
1082 induced seismicity in South Korea. *Science*, 360(6392), 1003-1006,
1083 <https://doi.org/10.1126/science.aat2010>.
1084

1085 Gischig, V. S. (2015). Rupture propagation behavior and the largest possible earthquake
1086 induced by fluid injection into deep reservoirs. *Geophysical Research Letters*, 42(18), 7420-
1087 7428, <https://doi.org/10.1002/2015GL065072>.
1088

1089 Gischig, V., Jalali, R., Amann, F., Krietsch, H., Klepikova, M., Esposito, S., ... & Madonna,
1090 C. (2016). Impact of the ISC Experiment at the Grimsel Test Site-Assessment of Potential
1091 Seismic Hazard and Disturbances to Nearby Experiments and KWO Infrastructure. *ETH
1092 Zurich Report*, <https://doi.org/10.3929/ethz-b-000189973>.
1093

1094 Gischig, V. S., Giardini, D., Amann, F., Hertrich, M., Krietsch, H., Loew, S., ... & Valley, B.
1095 (2020). Hydraulic stimulation and fluid circulation experiments in underground laboratories:
1096 Stepping up the scale towards engineered geothermal systems. *Geomechanics for Energy and
1097 the Environment*, 24, 100175, <https://doi.org/10.1016/j.gete.2019.100175>.
1098

1099 Guglielmi, Y., Cook, P., Soom, F., Schoenball, M., Dobson, P., & Kneafsey, T. (2021). In
1100 situ continuous monitoring of borehole displacements induced by stimulated hydrofracture
1101 growth. *Geophysical Research Letters*, 48(4), e2020GL090782,
1102 <https://doi.org/10.1029/2020GL090782>.
1103
1104 Gutenberg, B., & Richter, C. F. (1944). Frequency of earthquakes in California. *Bulletin of*
1105 *the Seismological Society of America*, 34(4), 185-188,
1106 <https://doi.org/10.1785/BSSA0340040185>.
1107
1108 Hanks, T. C., & Kanamori, H. (1979). A moment magnitude scale. *Journal of Geophysical*
1109 *Research: Solid Earth*, 84(B5), 2348-2350, <https://doi.org/10.1029/JB084iB05p02348>.
1110
1111 Hallo, M., Oprsäl, I., Eisner, L., & Ali, M. Y. (2014). Prediction of magnitude of the largest
1112 potentially induced seismic event. *Journal of Seismology*, 18, 421-431,
1113 <https://doi.org/10.1007/s10950-014-9417-4>.
1114
1115 Heise, J. (2015). The Sanford underground research facility at Homestake. In *Journal of*
1116 *Physics: Conference Series* (Vol. 606, No. 1, p. 012015). IOP Publishing,
1117 <https://doi.org/10.1088/1742-6596/606/1/012015>.
1118
1119 Holschneider, M., Zöller, G., & Hainzl, S. (2011). Estimation of the maximum possible
1120 magnitude in the framework of a doubly truncated Gutenberg–Richter model. *Bulletin of the*
1121 *Seismological Society of America*, 101(4), 1649-1659, <https://doi.org/10.1785/0120100289>.
1122
1123 Holschneider, M., Zöller, G., Clements, R., & Schorlemmer, D. (2014). Can we test for the
1124 maximum possible earthquake magnitude?. *Journal of Geophysical Research: Solid Earth*,
1125 119(3), 2019-2028, <https://doi.org/10.1002/2013JB010319>.
1126
1127 Im, K., & Avouac, J. P. (2025). Maximum Magnitude of Induced Earthquakes in Rate and
1128 State Friction Framework. *Seismological Research Letters*, 96(3), 1654-1664,
1129 <https://doi.org/10.1785/0220240382>.
1130
1131 Ishimoto, M., & Iida, K. (1939). Observations of earthquakes registered with the
1132 microseismograph constructed recently. *Bull. Earthq. Res. Inst. Univ. Tokyo*, 17, 443-478.
1133
1134 Jalali, M., Gischig, V., Doetsch, J., Näf, R., Krietsch, H., Klepikova, M., ... & Giardini, D.
1135 (2018). Transmissivity changes and microseismicity induced by small-scale hydraulic
1136 fracturing tests in crystalline rock. *Geophysical Research Letters*, 45(5), 2265-2273,
1137 <https://doi.org/10.1002/2017GL076781>.
1138
1139 Jin, G., Ning, Y., Gale, M., Simmons, J., & Tura, A. (2024). Impact of natural fractures on
1140 hydraulic fracture propagation in Denver-Julesburg Basin: Insights from a decade of research.
1141 *The Leading Edge*, 43(12), 806-814, <https://doi.org/10.1190/tle43120806.1>.
1142
1143 Kanamori, H., & Anderson, D. L. (1975). Theoretical basis of some empirical relations in
1144 seismology. *Bulletin of the Seismological Society of America*, 65(5), 1073-1095,
1145 <https://doi.org/10.1785/BSSA0650051073>.
1146
1147 Kass, R. E., & Raftery, A. E. (1995). Bayes factors. *Journal of the American Statistical*
1148 *Association*, 90(430), 773-795, <https://doi.org/10.1080/01621459.1995.10476572>.

1149
1150 Kettlety, T., Verdon, J. P., Butcher, A., Hampson, M., & Craddock, L. (2021). High-
1151 resolution imaging of the ML 2.9 August 2019 earthquake in Lancashire, United Kingdom,
1152 induced by hydraulic fracturing during Preston New Road PNR-2 operations. *Seismological*
1153 *Research Letters*, 92(1), 151-169, <https://doi.org/10.1785/0220200187>.
1154
1155 [Kijko, A. \(2025\). Bayesian Assessment of the Maximum Possible Earthquake Magnitude m](https://doi.org/10.17491/jgsi/2025/174157)
1156 [max. *Journal of the Geological Society of India*, 101\(6\), 764-769,](https://doi.org/10.17491/jgsi/2025/174157)
1157 <https://doi.org/10.17491/jgsi/2025/174157>.
1158
1159 Krietsch, H., Doetsch, J., Dutler, N., Jalali, M., Gischig, V., Loew, S., & Amann, F. (2018).
1160 Comprehensive geological dataset describing a crystalline rock mass for hydraulic
1161 stimulation experiments. *Scientific data*, 5(1), 1-12, <https://doi.org/10.1038/sdata.2018.269>.
1162
1163 Krietsch, H., Gischig, V., Evans, K., Doetsch, J., Dutler, N. O., Valley, B., & Amann, F.
1164 (2019). Stress measurements for an in situ stimulation experiment in crystalline rock:
1165 integration of induced seismicity, stress relief and hydraulic methods. *Rock Mechanics and*
1166 *Rock Engineering*, 52, 517-542, <https://doi.org/10.1007/s00603-018-1597-8>.
1167
1168 Krietsch, H., Villiger, L., Doetsch, J., Gischig, V., Evans, K. F., Brixel, B., ... & Amann, F.
1169 (2020a). Changing flow paths caused by simultaneous shearing and fracturing observed
1170 during hydraulic stimulation. *Geophysical Research Letters*, 47(3), e2019GL086135,
1171 <https://doi.org/10.1029/2019GL086135>.
1172
1173 Krietsch, H., Gischig, V. S., Doetsch, J., Evans, K. F., Villiger, L., Jalali, M., ... & Amann, F.
1174 (2020b). Hydromechanical processes and their influence on the stimulation effected volume:
1175 observations from a decameter-scale hydraulic stimulation project. *Solid Earth*, 11(5), 1699-
1176 1729, <https://doi.org/10.5194/se-11-1699-2020>.
1177
1178 Kroll, K. A., & Cochran, E. S. (2021). Stress controls rupture extent and maximum
1179 magnitude of induced earthquakes. *Geophysical Research Letters*, 48(11), e2020GL092148,
1180 <https://doi.org/10.1029/2020GL092148>.
1181
1182 Kneafsey, T. J., Dobson, P., Blankenship, D., Morris, J., Knox, H., Schwering, P., ... &
1183 Valladao, C. (2018). An overview of the EGS Collab project: field validation of coupled
1184 process modeling of fracturing and fluid flow at the Sanford Underground Research Facility,
1185 Lead, SD. In *43rd Workshop on Geothermal Reservoir Engineering* (Vol. 2018).
1186
1187 Kneafsey, T. J., Blankenship, D., Dobson, P. F., Morris, J. P., White, M. D., Fu, P., ... &
1188 Valladao, C. (2020). The EGS collab project: Learnings from Experiment 1. In *Proceedings*
1189 *of the 45th Workshop on Geothermal Reservoir Engineering* (pp. 10-12). Stanford, CA:
1190 Stanford University.
1191
1192 Kwiatek, G., Martínez-Garzón, P., Plenkers, K., Leonhardt, M., Zang, A., von Specht, S., ...
1193 & Bohnhoff, M. (2018). Insights into complex subdecimeter fracturing processes occurring
1194 during a water injection experiment at depth in Äspö Hard Rock Laboratory, Sweden.
1195 *Journal of Geophysical Research: Solid Earth*, 123(8), 6616-6635,
1196 <https://doi.org/10.1029/2017JB014715>.
1197

1198 Langenbruch, C., Moein, M. J., & Shapiro, S. A. (2024). Are maximum magnitudes of
1199 induced earthquakes controlled by pressure diffusion?. *Philosophical Transactions A*,
1200 382(2276), 20230184, <https://doi.org/10.1098/rsta.2023.0184>.
1201
1202 Lanza, F., Rinaldi, A.P., Passarelli, L., Ritz, V.A., Repollés, V.C., Schultz, R., Ciardo, F.,
1203 Dyer, B., Ermert, L., Grigoratos, I., Karvounis, D., Meier, P., Mignan, A., Moore, J. Pankow,
1204 K., Scarabello, L., Schmid, N., Shi, P., Tuinstra, K., & Wiemer, S. (2026). The 2022
1205 hydraulic stimulation at Utah FORGE: investigating fracturing mechanisms and testing
1206 forecasting approaches. Submitted to *Seismica*.
1207
1208 Lee, J., Tsai, V. C., Hirth, G., Chatterjee, A., & Trugman, D. T. (2024). Fault-network
1209 geometry influences earthquake frictional behaviour. *Nature*, 1-5,
1210 <https://doi.org/10.1038/s41586-024-07518-6>.
1211
1212 Li, Z., Elsworth, D., & Wang, C. (2021). Constraining maximum event magnitude during
1213 injection-triggered seismicity. *Nature Communications*, 12(1), 1528,
1214 <https://doi.org/10.1038/s41467-020-20700-4>.
1215
1216 Li, S., & Zhang, D. (2023). Three-dimensional thermoporoelastic modeling of
1217 hydrofracturing and fluid circulation in hot dry rock. *Journal of Geophysical Research: Solid*
1218 *Earth*, 128(2), e2022JB025673, <https://doi.org/10.1029/2022JB025673>.
1219
1220 López-Comino, J. Á., Cesca, S., Heimann, S., Grigoli, F., Milkereit, C., Dahm, T., & Zang,
1221 A. (2017). Characterization of hydraulic fractures growth during the Äspö Hard Rock
1222 Laboratory experiment (Sweden). *Rock Mechanics and Rock Engineering*, 50, 2985-3001,
1223 <https://doi.org/10.1007/s00603-017-1285-0>.
1224
1225 López-Comino, J. Á., Cesca, S., Niemz, P., Dahm, T., & Zang, A. (2021). Rupture directivity
1226 in 3D inferred from acoustic emissions events in a mine-scale hydraulic fracturing
1227 experiment. *Frontiers in Earth Science*, 9, 670757,
1228 <https://doi.org/10.3389/feart.2021.670757>.
1229
1230 Majer, E. L., Baria, R., Stark, M., Oates, S., Bommer, J., Smith, B., & Asanuma, H. (2007).
1231 Induced seismicity associated with enhanced geothermal systems. *Geothermics*, 36(3), 185-
1232 222, <https://doi.org/10.1016/j.geothermics.2007.03.003>.
1233
1234 Marzocchi, W., & Sandri, L. (2003). A review and new insights on the estimation of the b-
1235 value and its uncertainty. *Annals of Geophysics*, 46(6), 1271-1282.
1236
1237 Maurer, J., Dunham, E. M., & Segall, P. (2020). Role of fluid injection on earthquake size in
1238 dynamic rupture simulations on rough faults. *Geophysical Research Letters*, 47(13),
1239 e2020GL088377, <https://doi.org/10.1029/2020GL088377>.
1240
1241 McGarr, A. (2014). Maximum magnitude earthquakes induced by fluid injection. *Journal of*
1242 *Geophysical Research: solid earth*, 119(2), 1008-1019,
1243 <https://doi.org/10.1002/2013JB010597>.
1244
1245 McQuarrie, A. D. (1999). A small-sample correction for the Schwarz SIC model selection
1246 criterion. *Statistics & Probability Letters*, 44(1), 79-86, [https://doi.org/10.1016/S0167-](https://doi.org/10.1016/S0167-7152(98)00294-6)
1247 [7152\(98\)00294-6](https://doi.org/10.1016/S0167-7152(98)00294-6).

1248
1249 Mendeki, A.J., 2016. Mine Seismology Reference Book: Seismic Hazard: Institute of Mine
1250 Seismology, Tasmania, Australia. p 88. ISBN 978-0-9942943-0-2.
1251
1252 Moein, M. J., Langenbruch, C., Schultz, R., Grigoli, F., Ellsworth, W. L., Wang, R., ... &
1253 Shapiro, S. (2023). The physical mechanisms of induced earthquakes. *Nature Reviews Earth
1254 & Environment*, 4(12), 847-863, <https://doi.org/10.1038/s43017-023-00497-8>.
1255
1256 Moore, J., McLennan, J., Allis, R., Pankow, K., Simmons, S., Podgorney, R., ... & Rickard,
1257 W. (2019). The Utah Frontier Observatory for Research in Geothermal Energy (FORGE): an
1258 international laboratory for enhanced geothermal system technology development. In *44th
1259 Workshop on Geothermal Reservoir Engineering* (pp. 11-13). Stanford University.
1260
1261 Morris, J. P., Fu, P., Dobson, P., Ajo-Franklin, J., Kneafsey, T. J., Knox, H., ... & EGS
1262 Collab Team, _ . (2018). Experimental design for hydrofracturing and fluid flow at the DOE
1263 EGS collab testbed. In *ARMA US Rock Mechanics/Geomechanics Symposium* (pp. ARMA-
1264 2018). ARMA.
1265
1266 Muntendam-Bos, A. G., Hoedeman, G., Polychronopoulou, K., Draganov, D., Weemstra, C.,
1267 van der Zee, W., ... & Roest, H. (2022). An overview of induced seismicity in the
1268 Netherlands. *Netherlands Journal of Geosciences*, 101, e1,
1269 <https://doi.org/10.1017/njg.2021.14>.
1270
1271 Niemz, P., Cesca, S., Heimann, S., Grigoli, F., von Specht, S., Hammer, C., ... & Dahm, T.
1272 (2020). Full-waveform-based characterization of acoustic emission activity in a mine-scale
1273 experiment: a comparison of conventional and advanced hydraulic fracturing schemes.
1274 *Geophysical Journal International*, 222(1), 189-206, <https://doi.org/10.1093/gji/ggaa127>.
1275
1276 Niemz, P., Dahm, T., Milkereit, C., Cesca, S., Petersen, G., & Zang, A. (2021). Insights into
1277 hydraulic fracture growth gained from a joint analysis of seismometer-derived tilt signals and
1278 acoustic emissions. *Journal of Geophysical Research: Solid Earth*, 126(12), e2021JB023057,
1279 <https://doi.org/10.1029/2021JB023057>.
1280
1281 Niemz, P., Pankow, K., Isken, M.P., Whidden, K., McLennan, J., & Moore, J. (2025).
1282 Mapping fracture zones with nodal geophone patches: Insights from induced microseismicity
1283 during the 2024 stimulations at Utah FORGE. *Seismological Research Letters*,
1284 <https://doi.org/10.1785/0220240300>.
1285
1286 [Niemz, P., Petersen, G., Rutledge, J., Whidden, K., & Pankow, K. \(2026\). Isotropic
1287 components of microseismic moment tensors at Utah FORGE reveal a diversity of fluid
1288 pathway creation processes in EGS development. *Scientific Reports*,
1289 <https://doi.org/10.1038/s41598-026-42493-0>.](https://doi.org/10.1038/s41598-026-42493-0)
1290
1291 Norbeck, J. H., & Horne, R. N. (2018). Maximum magnitude of injection-induced
1292 earthquakes: A criterion to assess the influence of pressure migration along faults.
1293 *Tectonophysics*, 733, 108-118, <https://doi.org/10.1016/j.tecto.2018.01.028>.
1294
1295 Oldenburg, C., Dobson, P., Wu, Y., Cook, P., Kneafsey, T., Nakagawa, S., ... & Heise, J.
1296 (2017). Hydraulic fracturing experiments at 1500 m depth in a deep mine: Highlights from

1297 the kISMET project, in *42nd Workshop on Geothermal Reservoir Engineering*, p. 9, Stanford
1298 University.
1299
1300 Pisarenko, V. F., & Rodkin, M. V. (2022). Approaches to solving the maximum possible
1301 earthquake magnitude (Mmax) problem. *Surveys in Geophysics*, 1-35, doi:
1302 <https://doi.org/10.1007/s10712-021-09673-1>.
1303
1304 Qin, Y., Li, J., Huang, L., Schoenball, M., Ajo-Franklin, J., Blankenship, D., ... & EGS
1305 Collab Team. (2024). Source mechanism of kHz microseismic events recorded in multiple
1306 boreholes at the first EGS Collab testbed. *Geothermics*, 120, 102994,
1307 <https://doi.org/10.1016/j.geothermics.2024.102994>.
1308
1309 Rubin, A. M., Gillard, D., & Got, J. L. (1999). Streaks of microearthquakes along creeping
1310 faults. *Nature*, 400(6745), 635-641, <https://doi.org/10.1038/23196>.
1311
1312 Rutledge, J. T., Phillips, W. S., & Mayerhofer, M. J. (2004). Faulting induced by forced fluid
1313 injection and fluid flow forced by faulting: An interpretation of hydraulic-fracture
1314 microseismicity, Carthage Cotton Valley gas field, Texas. *Bulletin of the Seismological
1315 Society of America*, 94(5), 1817-1830, <https://doi.org/10.1785/012003257>.
1316
1317 Sáez, A., Passelègue, F., & Lecampion, B. (2025). Maximum size and magnitude of
1318 injection-induced slow slip events. *Science Advances*, 11(19), eadq0662,
1319 <https://doi.org/10.1126/sciadv.adq0662>.
1320
1321 Schneeberger, R., Kober, F., Spillmann, T., Blechschmidt, I., Lanyon, G. W., & Mäder, U. K.
1322 (2019). Grimsel Test Site: Revisiting the site-specific geoscientific knowledge. *Nagra
1323 Technical Report 19-01*. <https://nagra.ch/en/downloads/technical-report-ntb-19-01-2/>.
1324
1325 Schoenball, M., Ajo-Franklin, J., Fu, P., & Templeton, D. (2019). *Microseismic monitoring
1326 of meso-scale stimulations for the DOE EGS Collab project at the Sanford Underground
1327 Research Facility* (No. LLNL-CONF-767025). Lawrence Livermore National Lab.(LLNL),
1328 Livermore, CA (United States).
1329
1330 Schoenball, M., Ajo-Franklin, J. B., Blankenship, D., Chai, C., Chakravarty, A., Dobson, P.,
1331 ... & EGS Collab Team. (2020). Creation of a mixed-mode fracture network at mesoscale
1332 through hydraulic fracturing and shear stimulation. *Journal of Geophysical Research: Solid
1333 Earth*, 125(12), e2020JB019807, <https://doi.org/10.1029/2020JB019807>.
1334
1335 Schopper, F., Doetsch, J., Villiger, L., Krietsch, H., Gischig, V. S., Jalali, M., ... & Maurer,
1336 H. (2020). On the variability of pressure propagation during hydraulic stimulation based on
1337 seismic velocity observations. *Journal of Geophysical Research: Solid Earth*, 125(2),
1338 e2019JB018801, <https://doi.org/10.1029/2019JB018801>.
1339
1340 Schultz, R., Atkinson, G., Eaton, D. W., Gu, Y. J., & Kao, H. (2018). Hydraulic fracturing
1341 volume is associated with induced earthquake productivity in the Duvernay play. *Science*,
1342 359(6373), 304-308, <https://doi.org/10.1126/science.aao0159>.
1343
1344 Schultz, R., Skoumal, R. J., Brudzinski, M. R., Eaton, D., Baptie, B., & Ellsworth, W. (2020).
1345 Hydraulic fracturing-induced seismicity. *Reviews of Geophysics*, 58(3), e2019RG000695,
1346 <https://doi.org/10.1029/2019RG000695>.

Deleted: AGRA

1348
1349 Schultz, R., Beroza, G. C., & Ellsworth, W. L. (2021a). A risk-based approach for managing
1350 hydraulic fracturing-induced seismicity. *Science*, 372(6541), 504-507,
1351 <https://doi.org/10.1126/science.abg5451>.
1352
1353 Schultz, R., Beroza, G. C., & Ellsworth, W. L. (2021b). A strategy for choosing red-light
1354 thresholds to manage hydraulic fracturing induced seismicity in North America. *Journal of*
1355 *Geophysical Research: Solid Earth*, 126(12), e2021JB022340,
1356 <https://doi.org/10.1029/2021JB022340>.
1357
1358 Schultz, R., Ellsworth, W. L., & Beroza, G. C. (2022). Statistical bounds on how induced
1359 seismicity stops. *Scientific Reports*, 12(1), 1184, [https://doi.org/10.1038/s41598-022-05216-](https://doi.org/10.1038/s41598-022-05216-9)
1360 [9](https://doi.org/10.1038/s41598-022-05216-9).
1361
1362 Schultz, R., Baptie, B., Edwards, B., & Wiemer, S. (2023a). Red-light thresholds for induced
1363 seismicity in the UK. *Seismica*, 2(2), <https://doi.org/10.26443/seismica.v2i2.1086>.
1364
1365 Schultz, R., Park, Y., Aguilar Suarez, A. L., Ellsworth, W. L., & Beroza, G. C. (2023b). En
1366 echelon faults reactivated by wastewater disposal near Musreau Lake, Alberta. *Geophysical*
1367 *Journal International*, 235(1), 417-429, <https://doi.org/10.1093/gji/ggad226>.
1368
1369 Schultz, R., Ellsworth, W. L., & Beroza, G. C. (2023c). An ensemble approach to
1370 characterizing trailing-induced seismicity. *Seismological Research Letters*, 94(2A), 699-707,
1371 <https://doi.org/10.1785/0220220352>.
1372
1373 Schultz, R. (2024). Inferring maximum magnitudes from the ordered sequence of large
1374 earthquakes. *Philosophical Transactions A*, 382(2276), 20230185,
1375 <https://doi.org/10.1098/rsta.2023.0185>.
1376
1377 Schultz, R. (2025). Reining-in the spring-slider with reinforcement learning. *Journal of*
1378 *Geophysical Research: Solid Earth*, 130(3), e2024JB029697,
1379 <https://doi.org/10.1029/2024JB029697>.
1380
1381 Schultz, R., Lanza, F., Dyer, B., Karvounis, D., Fiori, R., Shi, P., Ritz, V., Villiger, L., Meier,
1382 P., & Wiemer, S. (2025). The bound growth of induced earthquakes could de-risk hydraulic
1383 fracturing, *Communications Earth & Environment*, [https://doi.org/10.1038/s43247-025-](https://doi.org/10.1038/s43247-025-02881-2)
1384 [02881-2](https://doi.org/10.1038/s43247-025-02881-2).
1385
1386 [Schultz, R. \(2026\). Improving the resolvability of \$M_{MAX}\$ truncation via deeper order statistics.](https://doi.org/10.1038/s43247-025-02881-2)
1387 [Geophysical Journal International](https://doi.org/10.1038/s43247-025-02881-2), [ggag110](https://doi.org/10.1038/s43247-025-02881-2), [https://doi.org/10.1038/s43247-025-](https://doi.org/10.1038/s43247-025-02881-2)
1388 [02881-2](https://doi.org/10.1038/s43247-025-02881-2).
1389
1390 Schwarz, G. (1978). Estimating the dimension of a model. *The Annals of Statistics*, 461-464.
1391
1392 Segall, P., & Lu, S. (2015). Injection-induced seismicity: Poroelastic and earthquake
1393 nucleation effects. *Journal of Geophysical Research: Solid Earth*, 120(7), 5082-5103,
1394 <https://doi.org/10.1002/2015JB012060>.
1395
1396 Shapiro, S. A., Dinske, C., Langenbruch, C., & Wenzel, F. (2010). Seismogenic index and
1397 magnitude probability of earthquakes induced during reservoir fluid stimulations. *The*
Leading Edge, 29(3), 304-309, <https://doi.org/10.1190/1.3353727>.

1398
1399 Shapiro, S. A., Krüger, O. S., Dinske, C., & Langenbruch, C. (2011). Magnitudes of induced
1400 earthquakes and geometric scales of fluid-stimulated rock volumes. *Geophysics*, 76(6),
1401 WC55-WC63, <https://doi.org/10.1190/geo2010-0349.1>.
1402
1403 Shapiro, S. A., Kim, K. H., & Rec, J. H. (2021). Magnitude and nucleation time of the 2017
1404 Pohang Earthquake point to its predictable artificial triggering. *Nature Communications*,
1405 12(1), 6397, <https://doi.org/10.1038/s41467-021-26679-w>.
1406
1407 Singh, A., Neupane, G., Dobson, P., Zoback, M., Morris, J., Fu, P., ... & Johnston, B. (2019).
1408 *Slip tendency analysis of fracture networks to determine suitability of candidate testbeds for*
1409 *the EGS Collab hydroshear experiment* (No. INL/CON-19-53585-Rev001). Idaho National
1410 Laboratory, Idaho Falls, United States.
1411
1412 Stanfors, R., Rhén, I., Tullborg, E. L., & Wikberg, P. (1999). Overview of geological and
1413 hydrogeological conditions of the Äspö hard rock laboratory site. *Applied Geochemistry*,
1414 14(7), 819-834, [https://doi.org/10.1016/S0883-2927\(99\)00022-0](https://doi.org/10.1016/S0883-2927(99)00022-0).
1415
1416 Stephansson, O., Semikova, H., Zimmermann, G., & Zang, A. (2019). Laboratory pulse test
1417 of hydraulic fracturing on granitic sample cores from Äspö HRL, Sweden. *Rock Mechanics*
1418 *and Rock Engineering*, 52, 629-633, <https://doi.org/10.1007/s00603-018-1421-5>.
1419
1420 Sugiura, N. (1978). Further analysis of the data by Akaike's information criterion and the
1421 finite corrections. *Communications in Statistics-Theory and Methods*, 7(1), 13-26,
1422 <https://doi.org/10.1080/03610927808827599>.
1423
1424 van der Elst, N. J., Page, M. T., Weiser, D. A., Goebel, T. H., & Hosseini, S. M. (2016).
1425 Induced earthquake magnitudes are as large as (statistically) expected. *Journal of*
1426 *Geophysical Research: Solid Earth*, 121(6), 4575-4590,
1427 <https://doi.org/10.1002/2016JB012818>.
1428
1429 Verdon, J. P., & Bommer, J. J. (2021). Green, yellow, red, or out of the blue? An assessment
1430 of Traffic Light Schemes to mitigate the impact of hydraulic fracturing-induced seismicity.
1431 *Journal of Seismology*, 25, 301-326, <https://doi.org/10.1007/s10950-020-09966-9>.
1432
1433 Verdon, J.P., Pullen, B., & Rodríguez-Pradilla, G. (2023). Growth and stabilisation of
1434 induced seismicity rates during long-term, low pressure fluid injection. *Philosophical*
1435 *Transactions A*, 382(2276), 20230183, <https://doi.org/10.1098/rsta.2023.0183>.
1436
1437 Verdon, J. P., & Eisner, L. (2024). An Empirically Constrained Forecasting Strategy for
1438 Induced Earthquake Magnitudes Using Extreme Value Theory. *Seismological Research*
1439 *Letters*, <https://doi.org/10.1785/0220240061>.
1440
1441 [Verdon, J. P., & Schultz, R. \(2026\). Induced earthquakes in the southern Delaware Basin,](#)
1442 [Texas, are bound by a geomechanically controlled maximum magnitude. *Geophysical*](#)
1443 [Research Letters](#), 53(3), e2025GL117419, <https://doi.org/10.1029/2025GL117419>.
1444
1445 Vigilante, P. J., Sone, H., Wang, H. F., Haimson, B., & Doe, T. W. (2017, June). Anisotropic
1446 strength of Poorman Formation rocks, kISMET project. In *ARMA US Rock*
1447 *Mechanics/Geomechanics Symposium* (pp. ARMA-2017). ARMA.

1448
1449 Villiger, L., Gischig, V. S., Doetsch, J., Krietsch, H., Dutler, N. O., Jalali, M., ... & Wiemer,
1450 S. (2020). Influence of reservoir geology on seismic response during decameter-scale
1451 hydraulic stimulations in crystalline rock. *Solid Earth*, 11(2), 627-655,
1452 <https://doi.org/10.5194/se-11-627-2020>.
1453
1454 Villiger, L., Gischig, V. S., Kwiatak, G., Krietsch, H., Doetsch, J., Jalali, M., ... & Wiemer, S.
1455 (2021). Metre-scale stress heterogeneities and stress redistribution drive complex fracture slip
1456 and fracture growth during a hydraulic stimulation experiment. *Geophysical Journal
1457 International*, 225(3), 1689-1703, <https://doi.org/10.1093/gji/ggab057>.
1458
1459 Wang, L., Kwiatak, G., Renard, F., Guérin-Marthe, S., Rybacki, E., Bohnhoff, M., ... &
1460 Dresen, G. (2024). Fault roughness controls injection-induced seismicity. *Proceedings of the
1461 National Academy of Sciences*, 121(3), e2310039121,
1462 <https://doi.org/10.1073/pnas.2310039121>.
1463
1464 Wagenmakers, E. J., & Farrell, S. (2004). AIC model selection using Akaike weights.
1465 *Psychonomic Bulletin & Review*, 11, 192-196, <https://doi.org/10.3758/BF03206482>.
1466
1467 White, M., Johnson, T., Kneafsey, T., Blankenship, D., Fu, P., Wu, H., ... & Zhang, Y. (2019,
1468 February). The necessity for iteration in the application of numerical simulation to EGS:
1469 Examples from the EGS Collab test bed 1. In *44th Workshop on Geothermal Reservoir
1470 Engineering*.
1471
1472 Waldhauser, F., Ellsworth, W. L., Schaff, D. P., & Cole, A. (2004). Streaks, multiplets, and
1473 holes: High-resolution spatio-temporal behavior of Parkfield seismicity. *Geophysical
1474 Research Letters*, 31(18), <https://doi.org/10.1029/2004GL020649>.
1475
1476 Wu, H., Fu, P., Morris, J. P., Mattson, E. D., Neupane, G., Smith, M. M., ... & EGS Collab
1477 Team. (2021a). Characterization of flow and transport in a fracture network at the EGS
1478 Collab field experiment through stochastic modeling of tracer recovery. *Journal of
1479 Hydrology*, 593, 125888, <https://doi.org/10.1016/j.jhydrol.2020.125888>.
1480
1481 Wu, H., Fu, P., Frone, Z., White, M. D., Ajo-Franklin, J. B., Morris, J. P., ... & EGS Collab
1482 Team. (2021b). Modeling heat transport processes in enhanced geothermal systems: A
1483 validation study from EGS Collab Experiment 1. *Geothermics*, 97, 102254,
1484 <https://doi.org/10.1016/j.geothermics.2021.102254>.
1485
1486 Yin, X., Jiang, C., Yin, F., Zhai, H., Zheng, Y., Wu, H., ... & Li, J. (2024). Assessment and
1487 optimization of maximum magnitude forecasting models for induced seismicity in enhanced
1488 geothermal systems: The Gonghe EGS project in Qinghai, China. *Tectonophysics*, 886,
1489 230438, <https://doi.org/10.1016/j.tecto.2024.230438>.
1490
1491 Yu, J., Eijssink, A., Marone, C., Rivière, J., Shokouhi, P., & Elsworth, D. (2024). Role of
1492 critical stress in quantifying the magnitude of fluid-injection triggered earthquakes. *Nature
1493 Communications*, 15(1), 7893, <https://doi.org/10.1038/s41467-024-52089-9>.
1494
1495 Zang, A., Zimmermann, G., Hofmann, H., Stephansson, O., Min, K. B., & Kim, K. Y.
1496 (2019). How to reduce fluid-injection-induced seismicity. *Rock Mechanics and Rock
1497 Engineering*, 52, 475-493, <https://doi.org/10.1007/s00603-018-1467-4>.

1498
1499 Zang, A., Zimmermann, G., Hofmann, H., Niemz, P., Kim, K. Y., Diaz, M., ... & Yoon, J. S.
1500 (2021). Relaxation damage control via fatigue-hydraulic fracturing in granitic rock as inferred
1501 from laboratory-, mine-, and field-scale experiments. *Scientific reports*, 11(1), 6780,
1502 <https://doi.org/10.1038/s41598-021-86094-5>.
1503
1504 Zang, A., Niemz, P., von Specht, S., Zimmermann, G., Milkereit, C., Plenkers, K., & Klee,
1505 G. (2024). Comprehensive data set of in situ hydraulic stimulation experiments for
1506 geothermal purposes at the Äspö Hard Rock Laboratory (Sweden). *Earth System Science*
1507 *Data*, 16(1), 295-310, <https://doi.org/10.5194/essd-16-295-2024>.
1508
1509 Zhou, W., Lanza, F., Grigoratos, I., Schultz, R., Cousse, J., Trutnevyte, E., Muntendam-Bos,
1510 A., & Wiemer, S. (2024). Managing induced seismicity risks from enhanced geothermal
1511 systems: A good practice guideline. *Reviews of Geophysics*,
1512 <https://doi.org/10.1029/2024RG000849>.
1513
1514 Zhuang, L., Kim, K. Y., Jung, S. G., Diaz, M., Min, K. B., Zang, A., ... & Hofmann, H.
1515 (2019). Cyclic hydraulic fracturing of pocheon granite cores and its impact on breakdown
1516 pressure, acoustic emission amplitudes and injectivity. *International Journal of Rock*
1517 *Mechanics and Mining Sciences*, 122, 104065, <https://doi.org/10.1016/j.ijrmms.2019.104065>.
1518
1519 Zimmermann, G., Zang, A., Stephansson, O., Klee, G., & Semiková, H. (2019). Permeability
1520 enhancement and fracture development of hydraulic in situ experiments in the Äspö Hard
1521 Rock Laboratory, Sweden. *Rock Mechanics and Rock Engineering*, 52, 495-515,
1522 <https://doi.org/10.1007/s00603-018-1499-9>.
1523
1524 Zöller, G., & Holschneider, M. (2016). The earthquake history in a fault zone tells us almost
1525 nothing about Mmax. *Seismological Research Letters*, 87(1), 132-137,
1526 <https://doi.org/10.1785/0220150176>.
1527
1528